Dependence of Ice Microphysical Properties On Environmental Parameters: Results from HAIC-HIWC Cayenne Field Campaign

Yachao Hu,[a,b] Greg M. McFarquhar,[b,c] Wei Wu,[b] Yongjie Huang,[c,h] Alfons Schwarzenboeck,[d] Alain Protat,[e] Alexei Korolev,[f] Robert M Rauber,[g] and Hongqing Wang[a]

[a]*Department of Atmospheric and Oceanic Sciences, School of Physics, Peking University, Beijing, China*

[b]*Cooperative Institute for Mesoscale Meteorological Studies, University of Oklahoma, Norman, Oklahoma, USA*

[c]*School of Meteorology, University of Oklahoma, Norman, Oklahoma, USA*

[d]*Laboratoire de Météorologie Physique, UCA, CNRS, Aubière, France*

[e]*Australian Bureau of Meteorology, Melbourne, Australia*

[f]*Environment and Climate Change Canada, Toronto, M3H 5T4, Canada*

[g]*Department of Atmospheric Sciences, University of Illinois at Urbana-Champaign, Urbana, IL, USA*

[h]*Center for Analysis and Prediction of Storms (CAPS), University of Oklahoma, Norman, Oklahoma, USA*

**Corresponding Author:*

Greg McFarquhar

Cooperative Institute for Mesoscale Meteorological Studies, University of Oklahoma

120 David L. Boren Blvd, Suite 2100

Norman, OK 73072

Email: mcfarq@ou.edu

Abstract

High Ice Water Content (HIWC) regions above tropical mesoscale convective systems are investigated using data from the second collaboration of the High Altitude Ice Crystals and High Ice Water Content projects (HAIC-HIWC) based in Cayenne, French Guiana in 2015. Observations from in-situ cloud probes on the French Falcon 20 determine the microphysical and thermodynamic properties of such regions. Data from a 2-D stereo probe and precipitation imaging probe show how statistical distributions of ice crystal mass median diameter (*MMD*), ice water content (*IWC*), and total number concentration (N_t) for particles with maximum dimension (D_{max}) > 55 µm vary with environmental conditions, temperature (*T*), and convective properties such as vertical velocity (*w*), MCS age, distance away from convective peak (*L*), and surface characteristics. *IWC* is significantly correlated with *w*, whereas *MMD* decreases and N_t increases with decreasing *T* consistent with aggregation, sedimentation and vapor deposition processes at lower altitudes. *MMD* typically increases with *IWC* when *IWC* < 0.5 g m^{-3}, but decreases with *IWC* when *IWC* > 0.5 g m^{-3} for -15 ºC ≤ *T* ≤ -5 ºC. Trends also depend on environmental conditions, such as presence of convective updrafts that are the ice crystal source, *MMD* being larger in older MCSs consistent with aggregation and less injection of small crystals into anvils, and *IWC*s decrease with increasing *L* at lower *T*. The relationship between *IWC* and *MMD* depends on environmental conditions, with correlations decreasing with decreasing *T*. The strength of correlation between *IWC* and N_t increases as *T* decreases.

1. Introduction

Clouds affect the dynamics and thermodynamics of the troposphere and are a key component in the energy balance and water cycle of Earth. The spatial and temporal distribution of clouds is inhomogeneous, making their representation one of the largest sources of uncertainty in climate models (e.g., Intergovernmental Panel on Climate Change, 2013; Chen et al., 2018). Mesoscale convective systems (MCSs), commonly defined as organized clusters of cumulonimbus clouds with contiguous precipitation regions over 100 km on a horizontal scale in at least one direction (Houze, 2014; Houze et al., 2019; Markowski and Richardson, 2010), are one of the most important types of convective systems on Earth.

Ice crystals found in cirrus and MCSs make important contributions to the radiative budget of Earth. The number distribution function (*N(D)*) is one of the important functions to describe microphysical properties of an ensemble of ice particles. *N(D)* is also referred to as Particle Size Distribution (*PSD*) and it allows assessment of total number concentration N_t, ice water content (*IWC*), mass-weighted terminal velocity v_m, effective radius R_e, and single scattering properties such as extinction β, many of which are prognosed or diagnosed in General Circulation Models (GCMs). Knowledge of ice crystal particle properties aids in the understanding of cloud microphysical processes and in the development of parameterizations of microphysical processes in GCMs (e.g., Stephens, 2005; Jakob and Klein, 1999; Sanderson et al., 2008; Jackson et al., 2015). For example, ice crystal fall speed, which is a function of crystal size assumed in ice cloud parameterizations, has a big effect on modeled cloud cover, life cycle, and radiative forcing (Sanderson et al., 2008). Mitchell et al. (2008) found that the GCMs predict a 12% increase in cloud ice amount and a 5.5% increase in cirrus cloud coverage globally when small ice crystals concentrations are increased due to the impact on ice sedimentation rates. Simulations from Boudala et al. (2007) including where contributions of crystals with mean effective size less than 150 μm had a net radiative forcing of 2.4 W m^{-2} greater than that of a control case where such contributions were excluded. McFarquhar and Black (2004) and others show knowledge of the size distribution is critical in determining the representation of sedimentation. In addition, knowledge of ice crystal sizes influences vertical profiles of radiative heating that affects the evolution of cloud systems and estimates of cloud radiative forcing (e.g., McFarquhar et al., 2000; 2003; Heymsfield and McFarquhar, 2002). Trends in how ice crystal properties vary with environmental conditions also give some indications of the microphysical processes that affect their evolution. Thus, knowledge about the controls of ice crystal properties articles can provide both process-oriented understanding of microphysical processes and improved parameterization of such processes for numerical models.

Aircraft measurements of the microphysical properties of tropical anvils generated by convection have been obtained in previous observational campaigns, including the Central Equatorial Pacific Experiment (CEPEX; McFarquhar and Heymsfield, 1996), the Texas and Florida Underflights (TEFLUN- A and -B) (Gage et al., 1999), the Brazil Large Scale Biosphere-Atmosphere Experiment (LBA) (Formenti et al., 2001), the Kwajalein, Marshall Islands Kwajalein Experiment (KWAJEX) (Heymsfield et al., 2002; Sobel et al., 2004), the Convection And Moisture EXperiment (CAMEX-4; Kakar et al., 2006), the Tropical Cloud Systems and Processes experiment (TCSP; Halverson et al., 2007), the Tropical Warm Pool International Cloud Experiment campaign (TWP-ICE; May et al., 2008), the National Aeronautic and Space Administration (NASA) African Monsoon Multidisciplinary Analysis (NAMMA; e.g., Heymsfield et al., 2009; Cifelli et al., 2010; Lawson et al., 2010; Bouniol et al., 2010, Mascio et al., 2020), and the Tropical Composition, Cloud, and Climate Coupling (TC4; e.g., Jensen et al., 2009; Toon et al., 2010； Lawson et al., 2010). Although prior studies have provided a wealth of cloud probe data for process understanding and parameterization development, only on rare occasions have *IWCs* larger than 1.5 g m^{-3} been measured, which is used here to designate high *IWC* (hereafter HIWC*)* regions. No distinction is made about the size of particles when defining HIWC regions. Although some previous studies used a threshold of 1.0 g m^{-3} to define HIWC regions (e.g., McFarquhar and Heymsfield, 1996; Lawson et al., 1998), HIWC conditions are defined here using a threshold of 1.5 g m^{-3} following the convention used for the HAIC/HIWC experiments (Leroy et al., 2016a, 2017; Strapp et al., 2020, 2021). Typically, measurements of high *IWCs* are hard to obtain because they are believed to occur close to convective cores where flying can be limited due safety reasons. Further, even when measurements have been made in HIWC regions, the measurements are highly uncertain because probes that measure bulk *IWC* tend to become saturated at high *IWC* (Davison et al., 2016; Strapp et al., 2016a) and estimates of *IWC* based on measured *PSDs* are highly uncertain without bulk measurements of *IWC* (e.g., McFarquhar et al., 2007a, Heymsfield et al., 2004; Lawson et al., 2010; Fontaine et al., 2014).

To overcome these difficulties, an international multi-agency collaboration called the High Altitude Ice Crystals (Dezitter et al., 2013) and High Ice Water Content (Strapp et al., 2016b) projects (HAIC-HIWC) organized multiple field campaigns to make microphysical measurements of HIWC conditions to investigate processes responsible for their occurrence. The particular focus of these experiments was to investigate regions with HIWC that were mainly composed of small crystals (area equivalent diameters < 300 μm) that had equivalent radar reflectivity values less than 30 dBZ and often lower than 20 dBZ for pilot X-band radar data (e.g., Lawson et al., 1998; Mason et al., 2006; Bravin et al., 2015; Fridlind et al., 2015; Wolde et al., 2016; Leroy et al., 2017). The effort consisted of 3 focused field campaigns in Feb. 2014 (HAIC-HIWC: Darwin, Australia; Leroy et al., 2017), May 2015 (HAIC-HIWC: Cayenne, French Guiana; Dezitter et al., 2013; Strapp et al., 2016b), and Aug. 2015 (HAIC-RADAR: Florida; Yost et al., 2018, Ratvasky et al., 2019). An overview of the total water content (*TWC*) and *PSD* microphysical results from these three campaigns, as applied to aviation regulatory issues, has been provided by Strapp et al. (2020). The data considerably extend those previously collected in cirrus outflows of tropical convection because of the focus on HIWC conditions and because a new bulk probe, the isokinetic evaporator probe (IKP2), was used to make more accurate measures of bulk mass in HIWC conditions.

Previous analysis of data collected during the Darwin campaign has shown that some HIWC (defined as $IWC > 1.5$ g m^{-3} irrespective of the sizes of particles) regions are indeed characterized by numerous small ice crystals. In particular, Leroy et al. (2017) found that in most cases ice crystals with area equivalent diameters (D_a) between 250 to 500 μm dominated the mass in the HIWC regions, similar to the findings of Fridlind et al. (2015) who used Airbus data to show HIWC regions had median D_a of 200 to 300 μm. However, in two other HAIC-HIWC cases the HIWC regions were dominated by ice crystals with D_a between 400 to 800 μm and up to 2 mm. Yost et al. (2018) used HAIC-HIWC data from all three campaigns, combined with geostationary satellite imager data, to develop a better climatology of HIWC conditions, showing the probability of HIWC occurrence depends on the proximity to an overshooting convective cloud top, the infrared brightness temperature at the tropopause and the daytime cloud optical depth.

Although these studies have provided a foundation on where HIWC regions occur, they are still not sufficient to explain the variability of ice properties. For example, strong vertical motions may transport ice crystal particles and tends to sort particles by size (Leroy et al., 2016a), different physical processes for different regions in MCS lead to different rain intensity at the surface and different radiative properties (Houze et al., 2004), and Bouniol et al. (2016) found the amounts of hydrometeors that are lifted to high altitudes vary with MCS lifecycle and vary for MCSs over three kinds of underlying surface characteristics (defined as whether the surface was land, ocean or coastline). Thus, examining the dependence of cloud properties on environmental conditions yields information about physical processes that are related to the production and distribution of ice crystal particles. Thus, the effect of these environmental conditions and properties of MCS (e.g., vertical motions, underlying surface characteristics were defined as whether the surface was land, ocean or coastline, age of convective system, and different regions in a convective system) are examined to see how they affect the properties of ice crystals and the frequency of occurrence of HIWC conditions dominated by small ice crystals.

Therefore this paper uses data obtained during the second HAIC-HIWC campaign conducted from 9–29 May 2015 out of Cayenne, French Guiana to investigate how the distributions of *IWC*, N_t, and Mass Median Diameters (*MMD*) vary with environmental conditions such as temperature (T), vertical velocity (w), underlying surface characteristics, the distance away from the peak of the convective core (L), the age of the convective system, and the Brightness Temperature Difference between two channels of 6.8 µm and 10.8 µm ($BTD_{6.8\text{-}10.8\mu m}$) that is correlated with the strength of convection system (e.g., Wu et al., 2016). Further, the dependence of *MMD* on *IWC* and the relationship between N_t and *IWC* as a function of these conditions are examined. The microphysical properties of the HIWC regions are also contrasted with observations obtained in regions without HIWCs. The rest of the paper is organized as follows. Section 2 describes the HAIC-HIWC dataset and methodology used to process the data. An example of a HIWC event is presented in section 3. Investigations of how the statistical distributions of *MMD*, *IWC*, and N_t vary with environmental conditions are shown in section 4. Section 5 summarizes the results and offers directions for future research.

2. Dataset and Methodology

The second HAIC-HIWC flight campaign was based out of Cayenne (French Guiana) 9-25 May 2015. Three aircraft were used: 1) the French Falcon 20, equipped with in-situ cloud probes, flew in convective systems at varying temperatures; 2) the National Research Council (NRC) Canadian Convair 580, equipped with in-situ cloud probes and the NRC Airborne W- and X-band (NAWX) Doppler dual-polarization radars (Wolde and Pazmany, 2005; Nguyen et al., 2019), flew mainly at a temperature level of -10 ºC; and 3) the Honeywell B757, flew outside of clouds at the altitudes the Falcon 20 was flying to evaluate new pilot radar detection algorithms of HIWC. Only the in-situ data acquired using the Falcon 20 are analyzed in this study to avoid any complications with different calibrations, probe functionally or processing algorithms that may affect the comparison of microphysical properties (McFarquhar et al., 2017). Comparing data from the same probe in different conditions is the most robust way to detect subtle differences in cloud properties.

Seventeen research flights, designated F10 through F26 were performed with the French Falcon 20 and are summarized in Table 1. The cloud measurements are sorted into three temperature levels: -10 ºC, -30 ºC, and -45 ºC as the flight strategies were mainly designed to acquire statistics on HIWCs at these altitudes. Three types of convective systems were sampled during HAIC-HIWC: two flights (F12, F26) sampled coastal convective systems; five flights (F10, F11, F15, F21, F25) sampled continental convective systems; and ten flights (F13, F14, F16, F17, F18, F19, F20, F22, F23, F24) sampled oceanic convective systems. The classification of these systems is defined according to the surface underlying the aircraft at the time of sampling.

a. Airborne Instrumentation

The in-situ instruments mounted on the Falcon 20 include a Cloud Droplet Probe version 2 (CDP-2), which nominally measures the *PSDs*, of cloud droplets between 2 µm and 50 µm from forward scattering of laser light of 785 nm wavelength (Lance et al., 2010), a 2-D stereo probe (2D-S) with 128 photodiodes and a photodiode resolution of 10 µm, and a precipitation imaging probe (PIP) with 54 photodiodes and a photodiode resolution of 100 µm. The 2D-S and PIP nominally measure hydrometers with sizes between 10 to 1280 µm and 100 to 6400 µm respectively by measuring particle size and shape from an array of photodiode detectors attached to fast response electronics (Lawson et al., 2006, Baumgardner et al., 2011, 2017). All particle probes were equipped with antishattering tips to mitigate the effect of ice particle shattering on measurements (Korolev et al., 2013a). The primary measurement of *TWC*, which is the sum of the *IWC* and liquid water content

(*LWC*), was made with IKP2 specially designed for this project for the high *TWC* environmental conditions (Davison et al., 2016; Strapp et al., 2016a). Secondary *TWC* measurements from a Science Engineering Associates (SEA) Robust hot wire *TWC* probe (Strapp et al., 2008; Grandin et al., 2014) provided backup and corroboration of IKP2 functionality. A Rosemount Icing Detector (Baumgardner and Rodi., 1989; Claffey et al., 1995; Cober et al., 2001), the CDP-2, and a *LWC* probe from SEA were used in combination to identify mixed-phase conditions and estimate *LWC* when at sufficient levels. A multi-beam 95GHz Doppler cloud radar (RAdar SysTem Airborne, RASTA) provided reflectivity and Doppler velocity (Protat et al., 2009; Leroy et al., 2016a). Temperature was measured by Rosemount 102 probe with an uncertainty of ± 1 ^{o}C. Vertical velocity was measured by Rosemount 858 5-hole pressure probe and transducers with an uncertainty of ± 0.3 m s^{-1} (Hartmann et al., 2018; Strapp et al., 2020). These two probes were installed on the French Falcon 20 and operated by the Service des Avions Francais Instrumentes pour la Recherche en Environnement (SAFIRE).

b. Data processing

1) Ice Water Content

The IKP2, specifically developed to measure the high *IWCs* expected during the HAIC-HIWC campaigns, was designed to measure condensed water contents up to 10 g m^{-3} at airspeeds of 200 m s^{-1} with an accuracy of at least 20% (Davison et al., 2008, 2016; Strapp et al., 2016a). Its isokinetic flow control ensures that liquid and ice particles are sampled at near unit efficiency without significant ice mass loss that is associated with bulk *TWC* hot-wire probes. *TWC* is estimated as the difference between the evaporated condensed water and background humidity. By subtracting the best estimate of humidity, assumed to be ice saturation to follow the method of Strapp et al. (2016a), data were generated for 5-second centered averages at 1-second spacing. The *TWC* is identical to *IWC* in the absence of liquid water, whose presence is inferred from a Rosemount Icing Detector (Baumgardner and Rodi, 1989). Cloud segments where the Rosemount Icing Detector frequency was decreasing and was lower than 40 kHz (Mazin et al., 2001) or *Nt* detected by CDP-2 larger than 10 cm^{-3} (Lance et al., 2010; Ding et al., 2020) identified the presence of *LWC* and occurred only 0.81% of the time. These data were removed from subsequent analysis to focus only on ice-phase conditions. To remove tenous clouds and consistent with the focus on HIWC clouds, only data with $IWC \geq 0.1$ g m^{-3} were used here. Maximum *IWCs* obtained by the IKP2 in Cayenne at different temperature levels for each flight are listed in Table 1.

2) Particle Size Distributions

Composite *PSDs* were derived from the 2D-S and PIP data, covering particle maximum dimensions (D_{max}) from 55 µm to 12845 µm at 10 µm resolution and representing 5-second averages (Leroy et al., 2017). The 5-second average represents a tradeoff between large numbers of particles for statistically significant sampling and fine resolution to resolve small-scale features of clouds (McFarquhar et al., 2007b). The best estimates of *PSDs* obtained using processing algorithms of Environment and Climate Change Canada and of the Université Blaise Pascal compared well against *PSD* generated using the University of Illinois/Oklahoma Optical Probe Processing Software (McFarquhar et al., 2017) for two 3-min periods from HAIC-HIWC, suggesting uncertainties in the processing algorithms were not affecting the derived *PSDs*. The processing algorithms assumed the sample area depended on the particle dimension along the photodiode array, included corrections for out-of-focus particles (Korolev 2007), and treated partially imaged particles following the approach of Heymsfield and Parrish (1978). *PSDs* were generated as functions of D_{max}, the length along the photodiode array and D_a. In this study, D_{max} is used to represent the particle dimension for easier comparison with prior studies and model parameterizations. Contributions from particles with D_{max} < 55 um are not included in the analysis because of large uncertainties associated with a size-dependent and poorly defined sample area (Baumgardner and Korolev, 1997; Korolev et al., 1998), and the possible inclusion of shattered artifacts not filtered by processing algorithms because of the higher airspeeds (Field et al., 2006; Korolev and Field, 2015). Previous studies have shown that *PSDs* from such sizes are highly uncertain (e.g., Jackson et al., 2015; McFarquhar et al., 2017). Data obtained by the CDP-2 are not considered here because the interpretation of its measurements in ice clouds is highly uncertain (McFarquhar et al., 2007a). The *IWC* and vertical velocity data were sorted into 5-second periods to match the integration period used for the *PSD* data.

3) Mass-size distribution

Particle mass is not measured by the imaging probes. A mass-dimensional (m-D_{max}) relation was used to estimate *IWC* from a *PSD*, where

$$m = \alpha D_{max}^{\beta} , \qquad (1)$$

with β varying in time according to measured crystal morphology following Leroy et al. (2016b, 2017), and α determined by forcing agreement between the *IWC* measured by the IKP2 and that derived from the *PSD*. The IKP2 was mounted on the left wing and *PSD* probes (2D-S and PIP) were mounted on the right wing of French Falcon 20 (the sight direction is from a vantage in front of and looking towards the plane; Strapp et al., 2020).

The mean airspeed of the aircraft is 170 m s^{-1} and *IWCs* measured by IKP2 vary by about 0.7% in 1-second. The spatial scale corresponding to 1-second (170 m) is much larger than the spatial scale corresponding to the distance between the probes, thus the uncertainty caused by the distance between the probes is much less than 0.7%. Further, the same particles are not sampled even if the probes are right next to each other. Thus, this factor was not included when calculating *MMD* due to the distance between probes is not a large source of uncertainty. The values of α (median: 0.0038) and β (median: 2.05) in the m-D_{max} relation are similar to those derived from previous studies, for example, α = 0.0070 and β = 2.2 for Heymsfield et al. (2010), α = 0.00257 and β = 2.0 for Cotton et al. (2013), α = 0.0054 and β = 2.05 for Fontaine et al. (2014), where D_{max} is in cm and α is in g $cm^{-\beta}$. Detailed flow of calculation for α and β can be referred to and Leroy et al. (2016b) and Strapp et al. (2020). *MMD* was derived as the dimension for which half the mass is contained in smaller particles and half in larger particles to follow previous studies (e.g., Fridlind et al., 2015; Leroy et al., 2017; Stanford et al., 2017; Strapp et al., 2020), and is represented numerically as follows:

$$\int_0^{MMD} \alpha D_{max}^{\beta}\, N(D_{max}) dD_{max} = \int_{MMD}^{\infty} \alpha D_{max}^{\beta}\, N(D_{max}) dD_{max} = \frac{1}{2} IWC. \quad (2)$$

Besides the influence of the m-D_{max} relationship, *MMD* is mainly controlled by the *PSDs* themselves. Sensitivity studies demonstrate that *MMD* is relatively insensitive to even very large increases in the concentrations of the smallest particle sizes (e.g., D_a < 50 μm) (Leroy et al., 2017). The omission of particles with D_{max} < 55 μm changed the calculated *MMD* by 0.76% on average compared to including these points. The mean absolute differences between the *MMDs* computed from different size definitions (D_{max}, the area equivalent diameter, the length along the photodiode array, and the mean chord length) vary between

30 and 50 µm (Leroy et al., 2016b). The *MMD* gives a good indication of whether or not the *PSDs* are dominated by small ice crystals.

4) Satellite Image Data

GOES-13 data are used to identify individual convective systems, and to determine the location of the aircraft within each MCS (e.g., the distance away from a convective core), and the age of the convective system. The GOES-13 data at spectral channels of 6.8 µm and 10.8 µm with a temporal resolution of 30 min are used here. The spatial resolution is about 4 km and the data are available over the domain of (0-10°N, 45-60°W) where the aircraft flew during the Cayenne campaign (https://doi.org/10.5065/D6NC5ZX6).

c. Methodology

1) Method of Identifying MCS and Age of MCS

The Brightness Temperature (*BT*) threshold used to define points inside MCSs has varied substantially in prior studies, ranging from 208K to 258K (e.g., Hodges and Thorncroft, 1997; Machado et al., 1998; Ai et al., 2016; Rafati and Karimi, 2017). Arkin and Meisner (1987) found that cloud tops with BT < 235K were associated with tropical rainfall so that a threshold of 235K has since been used to identify points contained within MCSs (Laurent et al., 2002; Vila et al., 2008). For this study, convective cloud candidates were first determined according to the definition of an MCS, which is defined to occur when the major axis of an area with the BT of the 10.8 µm channel ($BT_{10.8\mu m}$) < 235K is longer than 100 km (Kolios and Feidas, 2010; Chen et al., 2018). As the resolution of GOES-13 is about 4 km, this means the number of pixels along the major axis of the MCS identified area should be larger than 25. The function “boundaries” in MATLAB (Gonzalez, et al., 2004) was used to identify each MCS and connection needs to satisfy the condition that eight pixels are connected. If an identified region with temperature below 235K is peanut shaped with a very thin connection at the middle, it still satisfies this standard, and the major axis would be the full length of the peanut regardless of how narrow the connection is. Second, the time of MCS formation was defined as the time when at least one pixel of $BT_{10.8\mu m}$ became smaller than 235K, determined by examining the trajectory of the convective clouds' previous development visually. Third, the time of dissipation was defined as the time when $BT_{10.8\mu m}$ of all points in the system became greater than 235K by examining the trajectory of the convective clouds' subsequent development visually. At the initial time and time of dissipation, the principal axes of the MCS does not need to be greater than 100 km. All MCSs in this study are confined to the region (0-10°N, 45-60°W). The period from the initial time to the dissipating time is defined as the total lifetime of the convective system and the age of MCS can be calculated by using the actual time of the observation minus the initial time. Fourteen convective systems were identified for times corresponding to Falcon 20 observations and their properties are summarized in Table 1. The average lifetime of the 14 MCSs sampled was 22.6 h and the average age of the systems sampled was 10.6 h.

2) Calculation of the Distance to Convective Core

After determining the formation time and trajectory of the MCSs identified, the distance between the convective core and aircraft (*L*) was calculated. The method to determine *L* can be split into two steps. First, the coldest points of the MCS were identified by an algorithm. However, there could be many coldest points in different areas of a single MCS because a MCS can have multiple cores. In this case, the nearest and coldest point was defined as the convective core and used to calculate *L*. By analyzing the distributions of L and comparing with estimated L through scale on a map visually, the uncertainty of calculated L by algorithm is about 50 km in this study. Figure 1 shows an MCS identified at 15 May 2015 11:15:00 UTC, with the magenta triangle representing the location of aircraft and the cyan asterisk with $BT_{10.8\mu m}$ of 213.6K, denoting the convective core of the MCS. Following Chopde and Nichat (2013), the distance between the convective core and aircraft (L) was calculated as

$$L = 2(R + H)sin^{-1}\sqrt{sin^2(\frac{\emptyset_2-\emptyset_1}{2}) + cos(\emptyset_1)cos(\emptyset_2)sin^2(\frac{\theta_2-\theta_1}{2})}\ , \qquad (3)$$

where R is the radius of Earth assumed to be 6371 km, H is the height of aircraft above the sea level, and $\emptyset_2$ and $\emptyset_1$ represent the longitude of the convective core and aircraft respectively. θ_2 and θ_1 are the latitude of the convective core and aircraft respectively. The temporal resolution of the GOES-13 data is 30 minutes whereas the aircraft data are averaged to 5-second resolution. The in-situ data are matched to the GOES-13 data corresponding to the closest time so that the maximum time offset is 15 minutes. A total of 12,339 data points representing about 17.1 hours of data in different environmental conditions within organized MCSs as summarized in Table2.

3) $BTD_{6.8\text{-}10.8\mu m}$

Images of the infrared window at 10.8 µm are commonly used to derive motion vectors of cloudy areas in the troposphere (Nieman et al., 1997). Images of the water vapor channel at 6.7 µm are also used to determine upper troposphere motions in both cloudy and cloud-free environments (Velden et al., 1997). $BTD_{6.8\text{-}10.8\mu m}$ can be used to identify deep convective clouds because it takes large negative values for low-level clouds and its magnitude (absolute value) often decreases with rising cloud-top height, tending to zero near the tropopause (Donovan et al., 2008). By analyzing satellite observations and radiative transfer simulations, previous studies have found that $BTD_{6.8\text{-}10.8\mu m}$ can be positive when convective clouds penetrate the tropopause (Fritz and Laszlo, 1993; Ackerman, 1996; Levizzani and Setvák, 1996; Wu et al., 2016), so the value of $BTD_{6.8\text{-}10.8\mu m}$ can represent the strength of convection. The strength of convection can vary for different regions even in the same convective system, and microphysical processes may vary with local convective strength. Muhlbauer et al. (2014) investigated the relationship between cirrus microphysics and large-scale meteorology, finding that almost half of the cirrus cloud occurrences during the Department of Energy Small Particles in Cirrus (SPARTICUS) field campaign occurred in three distinct synoptic conditions, namely, upper-level ridges, midlatitude cyclones with frontal systems, and subtropical flows. The strength of convection varied for these systems. Thus, the value of $BTD_{6.8\text{-}10.8\mu m}$ at the aircraft location was used as a measured of the local convection intensity, and to investigate the effect of convective intensity on ice crystal properties.

d. Classification of Meteorological Conditions

To understand controls of the ice crystal properties in MCSs (*IWC*, N_t, and *MMD*) and to identify when HIWC conditions occur, each measurement was classified according to several different meteorological conditions as follows: 1) The temperature (T) was divided into three levels (-15 ºC $\leq T \leq$ -5 ºC; -35 ºC $\leq T \leq$ -25 ºC; -50 ºC $\leq T \leq$ -40 ºC) with most of the data concentrated on the temperatures of the constant altitude legs of -10 ºC, -30 ºC, and -45 ºC; 2) Three kinds of cloud vertical motions, updrafts, downdrafts, and stratiform regions, were considered. A convective updraft was defined as any 5-second period when w > 1 m s^{-1} was sustained for at least four consecutive seconds, and a downdraft was defined as any 5-second period when $w < -1$ m s^{-1} was sustained for at least four consecutive seconds (Jorgensen et al., 1985; McFarquhar and Black, 2004; Murphy et al., 2017). A stratiform (i.e., -1 m s$^{-1} \leq w \leq 1$ m s^{-1}) region was a period that had neither an updraft nor a downdraft present at the time of the observations. 3) The MCSs were separated into three groups according to whether the convection was over the ocean, coastline, or land (oceanic, coastal and continental MCS). 4) The distance between the aircraft and the convective core of MCS (L) determined whether the observations were collected near the convective core or at the edge of the convective system ($L \leq 50$ km, 50 km $< L \leq 100$ km, 100 km $< L \leq 200$ km, $L > 200$ km). 5) The MCS age was sorted into three groups (< 6h, 6-12h, > 12h) to investigate observations at different stages of MCS. 6) The brightness temperature difference ($BTD_{6.8\text{-}10.8\mu m}$), which gives a measure of the strength of local convection (Levizzani and Setvák, 1996; Wu et al., 2016), was divided into three groups ($BTD_{6.8\text{-}10.8\mu m}$ < -3K, -3 to -1K, > -1K). Different criteria for segregating according to L (e.g., intervals: 25 km, 100 km, and 200 km), MCS age (e.g., intervals: 3h and 5h), and $BTD_{6.8\text{-}10.8\mu m}$ (e.g., intervals: 2K, 3K, and 5K) were tested, and the results showed that variation of classification threshold had little effect on the conclusions reached on how the properties varied with environmental conditions. Table 2 lists the number of 5-second samples that are available for each of these environmental conditions.

3. Case Study: 15 May 2015

Figure 2 shows a time series of the microphysical properties measured by probes on the French Falcon 20 between 09:24:44 - 11:36:59 UTC on 15 May 2015 during F13. The Falcon 20 flew at three constant temperature levels within the organized MCS as shown in the upper panel (Fig. 2a), along with the distance between the aircraft and the convective core. Times segments when the Rosemount icing detector frequency was decreasing and was lower than 40 kHz and N_t measured by the CDP-2 was larger than 10 cm^{-3} are shaded by gray and cyan respectively and represent data assumed to be collected in clouds with liquid present. The *LWC* frequency was 0.64% for this event. This analysis focuses on three time periods. Period 1, marked by the black rectangle between 09:29:39 and 09:45:29 UTC in Figure 2c, shows a negative correlation coefficient of -0.76 (Pearson method, *p-value*: 10^{-36}) between *IWC* and *MMD*, with *MMD* between 400 and 800 µm when $IWC > 1.5$ g m^{-3}. The decrease of *MMD* with increasing *IWC* is consistent with the majority of cases during the Darwin campaign (Leroy et al., 2017), and shows these HIWC regions are mainly associated with small particles. On the other hand, *MMD* reached about 2000 µm when *IWC* decreases to 0.5 g m^{-3} at around 09:43 UTC. Another period of HIWC was sampled at a lower temperature level from -50 ºC $\leq T \leq$ -40 ºC. This HIWC event corresponds to measurements near the convective core as shown in period 2 marked by a blue rectangle between 11:01:04 and 11:11:04 UTC. This period is illustrated by the blue points that represent data with $IWC > 1.5$ g m^{-3} and $MMD < 400$ µm (Fig. 1). These data were obtained in a region with $BT_{10.8\mu m} < 235$K, which was near the peak of convection (marked by a cyan asterisk with $BT_{10.8\mu m} = 213.6$K), showing that processes within the convective core of this MCS were favorable for the generation of HIWC with small ice crystals. There are also time periods when small *MMD* occur in a region with $IWC < 0.5$ g m^{-3} as seen in period 3 marked by the green rectangle between 11:18:04 and 11:26:04 UTC in Figure 2c. This region exhibits a weak positive correlation coefficient of 0.29 (Pearson method, *p-value*: 0.016) between *IWC* and *MMD*, and shows that *MMD* can reach around 400 µm even when $IWC < 0.5$ g m^{-3}. In general, for the times with HIWCs, there are large

N_t (Fig. 2g), indicating a positive correlation between *IWC* and N_t. However, the relationship between N_t and *IWC* varies for different *T*. The HIWC regions typically occur for large updrafts and downdrafts as displayed in Figure 2d, similar to simulation results of Franklin et al. (2016) and Stanford et al. (2017), and to the observations of McFarquhar and Black (2004) and Mascio et al. (2020) that showed the *PSD* shape was influenced by *w*.

To summarize the findings from this case, the correlation between *IWC* and *MMD* was negative in the region with *IWC* > 1.5 g m^{-3}, whereas there was a positive correlation when *IWC* < 0.5 g m^{-3}. The convective core of the MCS was favorable for the generation of HIWC regions with small ice crystals. Other case studies were examined and showed similar results.

4. Statistical Analysis on Controls of HIWC regions

To better investigate where HIWC regions are likely to occur and to better investigate how environmental conditions control the microphysical properties of these regions, a statistical analysis of all data (12,339 points, ~17.1h) obtained by Falcon 20 during the Cayenne campaign was conducted. The conditions sampled during the 17 flights of the Cayenne HAIC-HIWC campaign are summarized in Table 1, including information on the *IWC* measured by IKP2 as a function of the temperature at flight level, the underlying surface conditions, and the initial and dissipation times of the MCS sampled. The data are separated into different groups according to temperature, vertical motion, underlying surface, distance away from the convective core, system age, and $BTD_{6.8\text{-}10.8\mu m}$ as discussed in Section 2. Table 2 shows the number of 5-second measurements that were obtained under each of these conditions.

a. Vertical velocity

In this section, distributions of *IWC*, *MMD* and N_t for different vertical motions (i.e, convective updrafts, downdrafts, and stratiform regions) are compared. Figure 3 (a, d, and g) shows the normalized frequency of occurrence of *IWC* for the three vertical motions as a function of *T*. The fractional frequency of occurrence of HIWC conditions, namely times when *IWC* > 1.5 g m^{-3}, is greater for updrafts than for downdrafts and stratiform regions. The frequency of HIWC points also decreases with decreasing *T*, with almost all (96.4%) *IWCs* measured in stratiform regions at -50 ºC ≤ *T* ≤ -40 ºC less than 1.5 g m^{-3}. Figure 3 (b, e, and h) shows the minimum, 5th, 25th, 50th, 75th, 95th, maximum, and mean *IWCs* for data obtained within the three vertical motions for different *T*. The violin plots give further information about the distribution of parameters. These plots again show that the *IWC* obtained in updrafts is larger than in downdrafts or stratiform regions. Almost 95% of *IWCs* obtained in updrafts are larger than 1.0 g m^{-3} for -15 ºC ≤ *T* ≤ -5 ºC, with the mean *IWC* larger than 1.0 g m^{-3} for all three *T*. Inferences about the physical processes occurring in the convection can be made from these findings. For example, this shows that the convective updrafts are the main source of the high *IWCs*. The *IWCs* in the stratiform regions are smaller than in updrafts or downdrafts. The *MMD* for the three cloud types shown in Figure 3 (c, f, and i) show that the *MMD* in updrafts are smaller than those in downdrafts and stratiform regions for *T* ≥ -15 ºC. The fact that the *IWCs* are very large in updrafts means that a lot of small ice crystals must be present in the updrafts and thus are being generated there by heterogeneous nucleation. On the other hand, there is no significant difference in *MMD* for the three vertical motions when *T* ≤ -25 ºC, with the difference in *MMD* between downdrafts and stratiform regions not passing the 5% significance level (figures not shown).

The normalized frequency of *MMD* for each *IWC* range for convective updrafts, downdrafts and stratiform regions is shown in Figure 4. The majority of *MMD* range from 400 to 1800 μm for -15 ºC ≤ T ≤ -5 ºC (Fig. 4l), 200 to 800 μm for -35 ºC ≤ T ≤ -25 ºC (Fig. 4h), and 150 to 600 μm for -50 ºC ≤ T ≤ -40 ºC (Fig. 4d). The ranges of *MMD* decrease sharply with decreasing T, consistent with the results of Leroy et al. (2016a) for the Cayenne campaign. The increase of *MMD* with increasing T is consistent with growth by aggregation and sedimentation of larger particles to lower altitudes. Further, the analysis is consistent with the sublimation of small ice crystals in subsaturated environments, keeping the concentration of ice crystals with D_{max} < 100 μm relatively low (Korolev et al., 2011; 2013b). The *MMD* increased with *IWC* when *IWC* < 0.5 g m^{-3} and *IWC* > 2.4 g m^{-3} at all three T, consistent with period 3 shown in Figure 2. However, the *MMD* decreased sharply with *IWC* for 0.5 < *IWC* ≤ 2.4 g m^{-3} at -15 ºC ≤ T ≤ -5 ºC (Fig. 4l) and slightly when T < -15 ºC. In general, *IWC* was positively correlated with *MMD* for stratiform regions when *IWC* < 0.5 g m^{-3}. In the convective updrafts the mean *MMD* of the updraft regions stayed around 500 μm for all three T, probably because the convective environment is more favorable for the generation of small ice crystals through heterogeneous or homogeneous nucleation. Further, particle collisions are more frequent given the higher N_t, suggesting many small ice crystals could be produced by secondary ice production processes (Korolev et al., 2020), perhaps for time periods when large supercooled drops are present.

Normalized 2-dimensional frequency distributions of N_t and *IWC* for updrafts, downdrafts and stratiform regions are shown in Figure 5. The relative uncertainty of N_t is typically around 50% and the maximum value N_t is about 2000 L^{-1} in this study. This value is smaller than the N_t reported by Fontaine et al. (2017), who found that most N_t for ice crystal diameters between 15 – 12,845 µm are less than 10^4 L^{-1} and sometimes on the order of 10^5 L^{-1} for data obtained from the Darwin HAIC/HIWC field campaign. The differences occur because Fontaine et al. (2017) included the concentrations of small crystals (< 55 µm) in the calculation of N_t, but the current study does not because particles in this size range have large but highly uncertain concentrations due to a small and poorly defined depth of field for such small particles (Korolev et al., 1998). The slope of the best fit line between IWC and N_t and R^2 increases with decreasing T. The N_t at the lower T are always larger than those at a higher T for the same IWC, meaning the relationship between N_t and T is negative. This is similar to the findings of Heymsfield et al. (2013) who noted the trend was a result of ice aggregation at lower altitude, and consistent with an increase of activity of ice nucleating particles with decreasing T (e.g., Fletcher, 2011; Cooper, 1986; Meyers et al., 1992; DeMott et al., 2010). On the other hand, Krämer et al. (2009) found a positive correlation between N_t and T. The N_t increase with IWC when IWC < 2.4 g m^{-3}, and decrease with IWC when IWC > 2.4 g m^{-3} at -15 ºC ≤ T ≤ -5 ºC, is consistent with Figure 4l and the presence of abundant small crystals in HIWC conditions. For the same IWC, N_t (updraft) > N_t (downdraft) > N_t (stratiform) when T > -35 ºC, with the similar slope for -50 ºC ≤ T ≤ -40 ºC. In general, there are significant differences between the updrafts and the other two regions, and less substantial differences between downdrafts and stratiform regions (figures not shown).

b. Surface characteristics beneath MCSs

Similar tests were conducted to determine whether the surfaces over which the aircraft flew were correlated with the microphysical distributions. The MCSs were divided into oceanic, coastal, and continental MCSs according to the underlying surface over which the flights occurred regardless of where the MCS originally formed. Figure 6 shows that *IWCs* in oceanic and coastal convective systems were usually greater than those in continental systems when -15 ºC ≤ T ≤ -5 ºC, as for example, 66.2% of points within coastal MCSs had *IWCs* larger than 1.0 g m^{-3}. But, *IWCs* in continental MCSs were greater than for the other two surface characteristics at -50 ºC ≤ T ≤ -40 ºC. The mean *MMD* in continental MCSs is the greatest, while the *MMD* in oceanic MCSs is the smallest at -15 ºC ≤ T ≤ -5 ºC. The two-sample Kolmogorov–Smirnov test method with a 5% significance level was applied in this study and there is not a significant difference in *MMD* when T ≤ -25 ºC for the different surface types. But, in general, the mean *MMD* decreases with decreasing T for the three surface conditions beneath MCSs. Figure 7 shows the normalized frequency of *MMD* for each *IWC* range for the different surfaces at three T. The *MMD* increase with *IWC* from 0.1 g m^{-3} to 0.5 g m^{-3} for oceanic and continental MCSs when -15 ºC ≤ T ≤ -5 ºC, but decrease sharply with *IWC* at the same T for coastal MCSs. *MMD* all increase with *IWC* from 0.1 g m^{-3} to 0.5 g m^{-3} for three kinds of MCSs when T ≤ -25 ºC.

Normalized 2-dimensional frequency distributions of N_t and *IWC* for the three types of surfaces are shown in Figure 8. The slopes of the best fit lines all increase with decreasing T. For the same *IWC*, N_t (oceanic) > N_t (coastal) > N_t (continental) when T ≥ -35ºC, while N_t (costal) < N_t (oceanic) < N_t (continental) when -50 ºC ≤ T ≤ -40 ºC. N_t doesn't change with *IWC* in a statistically significant fashion for continental systems when -15 ºC ≤ T ≤ -5 ºC. The slope of the fit line for the continental MCSs changes most with decreasing T, with the positive correlation between N_t and IWC becoming particularly significant (significance level $\alpha = 0.01$) at -50 ºC ≤ T ≤ -40 ºC. This means more small ice crystals are found in continental MCSs at the lower temperature levels, consistent with the convective available potential energy (CAPE) being greater over the mainland (~ 1386.4 J kg^{-1}) than over the ocean (~ 927.3 J kg^{-1}). The greater number of small crystals at the higher temperatures in the oceanic systems may be associated with the fact that convection is typically weaker over the oceans than over the continents (e.g., Lucas et al., 1994; Zipser et al., 2006; Matsui et al., 2016) so that they are not transported as far upwards. Differences in storm intensity and proximity to the convective core could have minimized the differences of distributions of *IWC* and *MMD* with respect to the variation with surface type (e.g., continent and ocean).

c. Distances away from the convective core

Lawson et al. (2010) found that *IWCs* in tropical anvil cirrus decrease with increasing distance away from the convection. Yost et al. (2018) also found that *IWCs* decrease as the distance away from overshooting tops increases. McFarquhar and Heymsfield (1996) found similar trends for three oceanic MCSs sampled. However, most of these studies were limited to distances approximately 100 km away from convective cores. In this section, the dependence of the microphysical properties with distance from the convective core as a function of T is analyzed by categorizing the data according to the distance between the aircraft and convective core, L, into four groups: ($L \leq 50$ km, 50 km $< L \leq 100$ km, 100 km $< L \leq 200$ km, and $L > 200$ km).

The mean *IWC* decreases with increasing L at -50 ºC ≤ T ≤ -40 ºC in Figure 9b, consistent with the analysis of period 2 in Figure 2. But different trends can be noted at the higher T, similar to the analysis of *IWCs* shown in Korolev et al. (2018). These results emphasize that the level must be accounted for when analyzing trends of *IWC* with L, something that was not accounted for in some previous studies. The *MMD* near the convective core are smaller than those further from the convective core at -15 ºC ≤ T ≤ -5 ºC, with a less significant difference when T ≤ -25 ºC. Figure 10 shows the normalized frequency of *MMD* for each *IWC* range for different L at three T. At -15 ºC ≤ T ≤ -5 ºC, the *MMD* increase with increasing *IWC* from 0.1 g m^{-3} to 0.5 g m^{-3}, and then decrease with increasing *IWC* when *IWC* > 0.5 g m^{-3} for the regions with L ≤ 100 km and L ≥ 200 km. However, the median *MMD* for 100 km < L ≤ 200 km stays between 800 μm and 1200 μm even when larger changes of *IWC* are noted. Thus, at -15 ºC ≤ T ≤ -5 ºC, the *MMD* obtained for 100 km < L ≤ 200 km are greater than for the other three regions for the same *IWC* when *IWC* > 0.5 g m^{-3}, perhaps because the environmental conditions within this region favor aggregation and sedimentation. In addition, as L increases the small-scale dynamical activity in the ice clouds (e.g., Lilly 1988) will play an increasingly important role in determining both *IWC* and *MMD* so that their distributions are less tied to the properties of the convection. Overall, *IWC* measured near the convective core is greater than those regions away from the convective core, due to spreading of the anvil, sublimation or aggregation of the smaller particles, and sedimentation of the larger particles.

Normalized 2-dimensional frequency distributions of N_t and *IWC* under different L are shown in Figure 11. The slopes of the fit lines increase with decreasing T for different L. The slope of the fit line is the smallest (79.6 g^{-1} m^{3} L^{-1}) for 100 km < L ≤ 200 km at -15 ºC ≤ T ≤ -5 ºC, corresponding to the median of *MMD* staying around 1000 μm even when *IWCs* change as shown in Figure 10k. This may mean ice crystals experience aggregation and sedimentation in this region to a greater extent than compared to other *L* regions at $-15\ ^{\circ}\mathrm{C} \leq T \leq -5\ ^{\circ}\mathrm{C}$, or alternatively, in-situ growth mechanisms due to internal dynamics may also be of importance. The role of ice particles generated in the convective core being transported and falling into this region because of advection of particles caused by horizontal wind effect must also be taken into account.

d. MCS age

Lawson et al (2010) found that *IWCs* in tropical anvil cirrus decrease with the age of the anvil. The impact of the MCS age on the distributions of *IWCs* and *MMD* is shown in Figure 12. The *IWC* in the 6-12h age is usually greater than in the < 6h and > 12h age when $T > -35\ ^{\circ}\mathrm{C}$. This is consistent with the 6-12h stage being in the developing or mature stage after ice has started being injected into the anvil (Leary and Houze, 1980), with many ice crystals being created and growing by aggregation. It is also noted that *IWCs* decrease with the increasing system age at $-50\ ^{\circ}\mathrm{C} \leq T \leq -40\ ^{\circ}\mathrm{C}$ most likely because the crystals are falling out from the higher levels of the anvil. The *IWC* in the > 12h age is the smallest, consistent with sublimation and a weakening and dissipation of MCSs not being conducive to the generation and growth of ice particles. The scatter in the data is no doubt associated with variations in the location of the measurements, variations in the intensity of the convection, and likely varying amounts of growth due to small-scale motions in the MCS. The mean *MMD* with < 6h age is smaller than those with MCS age > 6h when $-15\ ^{\circ}\mathrm{C} \leq T \leq -5\ ^{\circ}\mathrm{C}$, with no significant difference of *MMD* with MCS age shown at $T \leq -25\ ^{\circ}\mathrm{C}$. The smaller *MMD* for young MCSs is consistent with the generation of new particles that have not experienced appreciable growth with deposition, accretion or aggregation. Figure 13 shows the normalized frequency of *MMD* for each *IWC* range for different MCS ages at three T. The relationship between IWC and MMD is positive for MCS age > 6h when IWC < 0.5 g m^{-3} at -15 ºC ≤ T ≤ -5 ºC, while the MMD decrease continually with IWC from about 1600 μm to 400 μm for MCSs age < 6h at the same T. This is consistent with HIWC regions in the younger MCSs being dominated by small ice crystals nucleated within the active convection and subsequently being injected into the anvil. It is also noted that MMD for > 12h age is larger than age < 12h for the same IWC when IWC > 0.5 g m^{-3} at -15 ºC ≤ T ≤ -5 ºC.

Figure 14 shows normalized 2-dimensional frequency distributions of N_t and IWC as a function of MCS age. The slopes of the fit lines increase with decreasing T for different ages, especially it can increase from 155.7 g^{-1} m^3 L^{-1} at -15 ºC ≤ T ≤ -5 ºC to 590.4 g^{-1} m^3 L^{-1} at -50 ºC ≤ T ≤ -40 ºC in the MCS age with 6-12h. While the linear relationship does not increase significantly with decreasing T for the MCS age >12h, the distribution of frequency for MCS ages >12h at T ≤ -25 ºC shows two modes above and below the fit line, consistent with the weak positive relationship between IWC and MMD shown in Figure 14c and Figure 14f. Overall, for the same IWC, N_t among different MCSs ages shows that N_t (< 6h) > N_t (6-12h) > N_t (> 12h) for three T, meaning more small ice crystals are found in younger convective systems for the same $IWCs$, with numbers decreasing as the system ages consistent with the action of aggregation or a smaller rate of injection of small crystals into the anvil from active convection. Small-scale dynamical activity in the anvil cloud obfuscates some of these trends.

e. Effect of $BTD_{6.8\text{-}10.8\mu m}$

The $BTD_{6.8\text{-}10.8\mu m}$ at the location of the aircraft can reflect the local strength of convection as detected by GOES-13. In this section, the $BTD_{6.8\text{-}10.8\mu m}$ were separated into three groups (< -3K, -3 to -1K, and > -1K) at each T to investigate the effects of local convection strength on the microphysical properties. Figure 15 shows *IWCs* and *MMD* distributions for different $BTD_{6.8\text{-}10.8\mu m}$ at three T. The *IWCs* increase with increasing $BTD_{6.8\text{-}10.8\mu m}$ for three T, indicating stronger convection favors the generation of more mass of ice crystals. However, *MMD* shows no significant difference with $BTD_{6.8\text{-}10.8\mu m}$ at all three T. This could be associated with the lifting of large amounts of hydrometeors to a high altitude in regions of strong convection (Bouniol et al., 2016), with the nucleation of more particles there. Figure 16 shows the normalized frequency of *MMD* for each *IWC* range as a function of $BTD_{6.8\text{-}10.8\mu m}$ at three T. The trends of *MMD* with increasing *IWC* between different groups of $BTD_{6.8\text{-}10.8\mu m}$ are not significantly different, showing the strength of the convection does not seem to affect the size of the crystals generated.

Normalized 2-dimensional frequency distributions of N_t and *IWC* for different $BTD_{6.8\text{-}10.8\mu m}$ are shown in Figure 17. The slopes of the fit lines all increase with decreasing T for different $BTD_{6.8\text{-}10.8\mu m}$. For the same *IWC*, N_t among different groups of $BTD_{6.8\text{-}10.8\mu m}$ shows that N_t (< -3K) > N_t (-3 to -1K) > N_t (> -1K) at -50 ºC ≤ T ≤ -40 ºC, while the results are N_t (-3 to -1K) > N_t (> -1K) > N_t (< -3K) at -35 ºC ≤ T ≤ -25 ºC, and no statistically significant difference is noted for three groups at -15 ºC ≤ T ≤ -5 ºC. Thus, there seem to be no clear trends on how the strength of the convection affects the sizes of the crystals.

5. Conclusions

The variation of distributions of microphysical parameters, such as ice water content (*IWC*), total number concentrations (N_t), and mass median diameter (*MMD*) with environmental conditions was examined using data obtained during the second HAIC-HIWC flight campaign conducted from 9-29 May 2015 out of Cayenne, French Guiana.

Data were separated according to temperature (T, -15 ºC ≤ T ≤ -5 ºC; -35 ºC ≤ T ≤ -25 ºC; -50 ºC ≤ T ≤ -40 ºC), vertical velocity (updrafts, downdrafts, and stratiform cloud regions), surface conditions (oceanic, coastal and continental), distance away from the convective core ($L \leq 50$ km, 50 km < $L \leq 100$ km, 100 km < $L \leq 200$ km, $L > 200$ km), MCS age (< 6h, 6-12h, > 12h), and convective strength ($BTD_{6.8\text{-}10.8\mu m}$ < -3K, -3 to -1K, > -1K). A paired test was used to test for statistically significant differences between distributions as functions of these environmental conditions. The difference of microphysical properties between the HIWC region was also contrasted against those obtained in regions without HIWCs. The principal findings of this study are as follows:

1. T has highest correlation with IWC and MMD. High $IWCs$ are more likely to occur at higher T. MMD are mainly in the range of 400-1800 µm for -15 ºC ≤ T ≤ -5 ºC, 200-800 µm for -35 ºC ≤ T ≤ -25 ºC, and 150-600 µm for -50 ºC ≤ T ≤ -40 ºC, showing a sharp decrease with decreasing T. The negative correlation between N_t and T noted is consistent with ice particle growth by vapor deposition and aggregation during descent in anvils.
2. At -15 ºC ≤ T ≤ -5 ºC, MMD increase with increasing IWC when IWC < 0.5 g m^{-3}, decrease when 0.5 g m^{-3} < IWC < 2.4 g m^{-3}, and are the smallest for IWC > 2.4 g m^{-3} for most environmental conditions (e.g., updrafts and downdrafts, coastal and continental MCS, MCS age < 12h, and $BTD_{6.8\text{-}10.8\mu m}$ < -3K). This shows that the HIWC regions are dominated by small ice crystals. There are some regions with exceptions to these trends (e.g., MMD does not vary significantly with IWC for 100 km ≤ L ≤ 200 km, and MMD increases with IWC for system age > 12h when T ≤ -25 ºC). The strength of dependence of the

relationship between *IWC* and *MMD* on environmental conditions decreases with decreasing *T*.

3. The distributions of *IWC* are statistically correlated with the strength of vertical velocity. HIWC regions usually occur for large upward *w* or downward *w*. *IWC* in updrafts is likely to be larger than in downdrafts and stratiform clouds at all *T*, meaning the convective environment is more favorable for the nucleation of small ice crystals.
4. More small ice crystals are found in continental MCSs at lower *T*, consistent with the convection being more intense over the mainland.
5. *IWCs* for MCS ages between 6-12h at higher *T* are the largest. Most MCSs with ages between 6-12h are in the mature stage, and hence there is significant outflow of fresh particles to the surrounding regions. Ice crystals may experience more aggregation and deposition growth in older MCSs with less outflow, explaining why *MMD* are larger in older MCSs.
6. For -50 ºC ≤ *T* ≤ -40 ºC, *IWC* is highly correlated to distance from the convective core, with *IWC* decreasing with increasing *L*. HIWC regions can exist around the convective core and the regions away from the convective core for -15 ºC ≤ *T* ≤ -5 ºC, consistent with the analysis of Korolev et al. (2018).
7. *IWCs* increase with increasing $BTD_{6.8\text{-}10.8\mu m}$ at different *T* whereas *MMD* show no significant differences for different $BTD_{6.8\text{-}10.8\mu m}$, meaning the more intense convection generates more ice, but does not necessarily affect the sizes of the particles generated.

8. The strength of correlations between N_t and IWC all increases with decreasing T for different environmental conditions, and the dependence of N_t on IWC varies with environmental conditions at the same T.

The findings presented here apply only to data collected in the vicinity of Cayenne, French Guiana during HAIC-HIWC. Future studies should concentrate on analysis of data collected in more diverse geographic locations, and should seek to obtain more data in updrafts and downdrafts where there are still little data. Such data would permit better statistical analysis of how the microphysical characteristics of HIWC clouds vary with a range of environmental conditions to provide further insight into the microphysical processes that occur in tropical ice clouds. Model simulations evaluated with the HAIC-HIWC data can also provide this insight because applying different microphysical parameterizations in the model makes it possible to investigate the microphysical processes that are most responsible for generating large amounts of small ice crystals (e.g., Huang et al., 2021). Extending the analysis presented here to retrievals of *IWC* from dual-polarization radar data (X and W band) evaluated against in-situ data acquired during the project can also extend the amount of data available for the analysis (Nguyen et al., 2019).

Acknowledgments: This work was supported by the National Science Foundation (Award Numbers: 1213311 and 1842094). Observation data are provided through NCAR/EOL under the sponsorship of the National Science Foundation (https://data.eol.ucar.edu/). NCAR is sponsored by the National Science Foundation. Major North American funding for flight campaigns was provided by the FAA William Hughes Technical Center and

Aviation Weather Research Program, the NASA Aeronautics Research Mission Directorate Aviation Safety Program, the Boeing Co., Environment and Climate Change Canada, the National Research Council of Canada, and Transport Canada. Major European campaign and research funding was provided from (i) the European Commission Seventh Framework Program in research, technological development and demonstration under grant agreement ACP2-GA-2012-314314, (ii) the European Safety Agency (EASA) Research Program under service contract EASA.2013.FC27. Operational support for the research aircraft Falcon 20 was provided by the SAFIRE facility for the scientific airborne operations. SAFIRE (http://www.safire.fr), is a joint facility of CNRS, Météo-France and CNES. Further funding was provided by the Ice Crystal Consortium. Some of the computing for this project was performed at the University of Oklahoma (OU) Supercomputing Center for Education and Research (OSCER). The discussions of HIWC conditions and aircraft measurements with Walter Strapp are greatly appreciated. The first author is also supported by the China Scholarship Council (CSC). The authors are also grateful to three anonymous reviewers who provided helpful comments and suggestions that improved the manuscript.

References

Ackerman, S. A., 1996: Global satellite observations of negative brightness temperature differences between 11 and 6.7 μm. *J. Atmos. Sci.*, **53,** 2803–2812, https://doi.org/10.1175/1520-0469(1996)053<2803:GSOONB>2.0.CO;2.

Ai, Y. F., W. B. Li, Z. Y. Meng, and J. Li, 2016: Life cycle characteristics of MCSs in middle east China tracked by geostationary satellite and precipitation estimates, *Mon. Wea. Rev.*, **144,** 2517-2530, https://doi.org/10.1175/MWR-D-15-0197.1.

Arkin, P. A., and Meisner, B. N. 1987: The relationship between large-scale convective rainfall and cold cloud over the Western Hemisphere during 1982-84. *Mon. Wea. Rev.*, **115,** 51-74, https://doi.org/10.1175/1520-0450(1997)036%3C0234:EOPAAR%3E2.0.CO;2.

Baumgardner, D., and Rodi, A., 1989: Laboratory and Wind Tunnel Evaluations of the Rosemount Icing Detector, *J. Atmos. Oceanic Technol.*, **6,** 971-979, https://doi.org/10.1175/1520-0426(1989)006<0971:LAWTEO>2.0.CO;2.

Baumgardner, D., and A. Korolev, 1997: Airspeed Corrections for Optical Array Probe Sample Volumes. *J. Atmos. Oceanic Technol.*, **14,** 1224-1229, https://doi.org/10.1175/1520-0426(1997)014<1224:ACFOAP>2.0.CO;2.

Baumgardner, D., Brenguier, J. L., Bucholtz, A., Coe, H., DeMott, P., Garrett, T. J., Gayet,J. F., Hermann, M., Heymsfield, A., Korolev, A., Krämer, M., Petzold, A., Strapp, W., Pilewskie, P., Taylor, J., Twohy, C., Wendisch, M., Bachalo, W., and Chuang, P., 2011: Airborne instruments to measure atmospheric aerosol particles, clouds and radiation: A cook's tour of mature and emerging technology. *Atmos. Res.*, **102,** 10–29, https://doi.org/10.1016/j.atmosres.2011.06.021.

Baumgardner, D., Abel, S. J., Axisa, D., Cotton, R., Crosier, J., Field, P., Gurganus, C., Heymsfield, A., Korolev, A., Krämer, M., Lawson, P., McFarquhar, G., Ulanowski, Z., and Um, J., 2017: Cloud Ice Properties: In Situ Measurement Challenges. *Meteorological Monographs.*, **58,** 9.1-9.23. https://doi.org/10.1175/AMSMONOGRAPHS-D-16-0011.1.

Boudala, F. S., Isaac, G. A., McFarlane, N. A., and Li, J., 2007: The sensitivity of the radiation budget in a climate simulation to neglecting the effect of small ice particles. *J. Climate*, **20**, 3527–3541, doi:10.1175/JCLI4191.1.

Bouniol, D., J. Delanoë, C. Duroure, A. Protat, V. Giraud, and G. Penide, 2010: Microphysical characterization of West African MCS anvils. *Quart. J. Roy. Meteor. Soc.*, **136,** 323–344, https://doi.org/10.1002/qj.557.

Bouniol, D., Roca, R., Fiolleau, T., and Poan, D. E., 2016: Macrophysical, microphysical, and radiative properties of tropical mesoscale convective systems over their life cycle. *J. Climate*, ***29*,** 3353-3371, https://doi.org/10.1175/JCLI-D-15-0551.1.

Bravin, M., J.W. Strapp, and J. Mason, 2015: An investigation into location and convective lifecycle trends in an ice crystal icing engine database, *Tech. rep.*, *SAE Technical Paper*. [Available online at https://doi.org/10.4271/2015-01-2130.]

Chen, D., Guo, J., Wang, H., Li, J., Min, M., Zhao, W., and Yao, D., 2018: The cloud top distribution *and* diurnal variation of clouds over East Asia: Preliminary results from Advanced Himawari Imager. *J. Geophys. Res.*, **123,** 3724–3739, https://doi.org/10.1002/2017JD028044.

Chopde, N. R., and Nichat, M., 2013: Landmark based shortest path detection by using A* and Haversine formula. *International Journal of Innovative Research in Computer and Communication Engineering*, **1,** 298-302. [Available online at https://www.researchgate.net/profile/Mangesh-Nichat-2/publication/282314348_Landmark_based_shortest_path_detection_by_using_A_Algorithm_and_Haversine_Formula/links/56389bb708ae4bde5021b0f5/Landmark-based-shortest-path-detection-by-using-A-Algorithm-and-Haversine-Formula.pdf.]

Cifelli, R., T. Lang, S. A. Rutledge, N. Guy, E. J. Zipser, J. Zawislak, and R. Holzworth, 2010: Characteristics of an African Easterly Wave Observed during NAMMA. *J. Atmos. Sci.*, **67**, 3–25, https://doi.org/10.1175/2009JAS3141.1.

Claffey, K. J., K. F. Jones, and C. C. Ryerson, 1995: Use and calibration of Rosemount ice detectors for meteorological research. *Atmos. Res.*, **36,** 277–286, https://doi.org/10.1016/0169-8095(94)00042-C.

Cober, S. G., G. A. Isaac, and A. V. Korolev, 2001: Assessing the Rosemount Icing Detector with in situ measurements. *J. Atmos. Oceanic Technol.*, **18,** 515–528, https://doi.org/10.1175/1520-0426(2001)018<0515:ATRIDW>2.0.CO;2.

Cooper W. A., 1986: Ice Initiation in Natural Clouds. Precipitation Enhancement—A Scientific Challenge. *Meteorological Monographs., Am. Meteor. Soc.,* Boston, MA., **21,** pp 29–32. [Available online at https//link.springer.com/chapter/10.1007/978-1-935704-17-1_4.]

Cotton, R. J., Field, P. R., Ulanowski, Z., Kaye, P. H., Hirst, E., Greenaway, R. S., Crawford, I., Crosier, J., and Dorsey, J., 2013: The effective density of small ice particles obtained from in situ aircraft observations of mid-latitude cirrus, *Q. J. Roy. Meteorol. Soc.*, **139,** 1923–1934, https://doi.org/10.1002/qj.2058.

Davison, C. R., J. MacLeod, J. Strapp, and D. Buttsworth, 2008: Isokinetic total water content probe in a naturally aspirating configuration: Initial aerodynamic design and testing. *Proc. 46th AIAA Aerospace Sciences Meeting and Exhibit,* Reno, NV, American Institute of Aeronautics and Astronautics, AIAA-2008-435. [Available online at http://arc.aiaa.org/doi/ abs/10.2514/6.2008-435.]

Davison. C.R., J.W. Strapp, L.E. Lilie, T.P. Ratvasky, and C. Dumont, 2016: Isokinetic TWC evaporator probe: Calculations and systemic error analysis. *Eighth AIAA Atmospheric and Space Envrionments Conf.*, Washington, DC, American Institute of Aeronautics and Astronautics, AIAA-2016-4060. [Available online at http://arc.aiaa.org/doi/10.2514/6.2016-4060.]

DeMott, P. J., Prenni, A. J., Liu, X., Kreidenweis, S. M., Petters, M. D., Twohy, C. H., M. Richardson, S., Eidhammer, T., and Rogers, D., 2010: Predicting global atmospheric ice nuclei distributions and their impacts on climate. *Proc. Natl. Acad. Sci. U. S. A.,**107***, 11217-11222. https://doi.org/10.1073/pnas.0910818107.

Dezitter, F., A. Grandin, J. L. Brenguier, F. Hervy, H. Schlager, P. Villedieu, and G. Zalamansky, 2013: HAIC (High altitude ice crystals). *Proc. Fifth AIAA Atmospheric and Space Environments Conf.,* San Diego, CA, American Institute of Aeronautics and Astronautics, AIAA-2013-2674. [Available online at http://arc.aiaa.org/doi/abs/10.2514/6.2013-2674.]

Ding, S., McFarquhar, G. M., Nesbitt, S. W., Chase, R. J., Poellot, M. R., and Wang, H., 2020: Dependence of Mass—Dimensional Relationships on Median Mass Diameter. *Atmosphere*, **11,** 756. https://doi.org/10.3390/atmos11070756.

Donovan, M. F., E. R. Williams, C. Kessinger, G. Blackburn, P. H. Herzegh, R. L. Bankert, S. Miller, and F. R. Mosher, 2008: The identification and verification of hazardous convective cells over oceans using visible and infrared satellite observations. *J. Appl. Meteor. Climatol.*, **47,** 164–184, https://doi.org/10.1175/2007JAMC1471.1.

Field, P. R., A. J. Heymsfield, and A. Bansemer, 2006: Shattering and Particle Interarrival Times Measured by Optical Array Probes in Ice Clouds. *J. Atmos. Oceanic Technol.*, **23,** 1357–1371, https://doi.org/10.1175/JTECH1922.1.

Fletcher, N. H., 2011: The physics of rainclouds. *Cambridge University Press*. [Available online at https://cds.cern.ch/record/2051935.]

Fontaine, E., A. Schwarzenboeck, J. Delanoë, W. Wobrock, D. Leroy, R. Dupuy, C. Gourbeyre, and A. Protat, 2014: Constraining mass–diameter relations from hydrometeor images and cloud radar reflectivities in tropical continental and oceanic convective anvils. *Atmos. Chem. Phys.*, **14,** 11367–11392, https://doi.org/10.5194/acp-14-11367-2014.

Fontaine, E., Leroy, D., Schwarzenboeck, A., Delanoë, J., Protat, A., Dezitter, F., Grandin, A., Strapp, J. W., and Lilie, L. E., 2017: Evaluation of radar reflectivity factor simulations of ice crystal populations from in situ observations for the retrieval of condensed water content in tropical mesoscale convective systems, *Atmos. Meas. Tech.*, **10,** 2239–2252, https://doi.org/10.5194/amt-10-2239-2017.

Formenti, P., Andreae, M. O., Lange, L., Roberts, G., Cafmeyer, J., Rajta, I., Holben, B.N., Artaxo, P., Maenhaut, W., and Lelieveld, J., 2001: Saharan dust in Brazil and Suriname during the Large-Scale Biosphere-Atmosphere Experiment in Amazonia (LBA)-Cooperative LBA Regional Experiment (CLAIRE) in March 1998. *J. Geophys. Res.*, **106,** 14919-14934, https://doi.org/10.1029/2000JD900827.

Franklin, C. N., Protat, A., Leroy, D., and Fontaine, E., 2016: Controls on phase composition and ice water content in a convection-permitting model simulation of a tropical mesoscale convective system, *Atmos. Chem. Phys.*, **16,** 8767–8789, https://doi.org/10.5194/acp-16-8767-2016.

Fridlind, A., A. Ackerman, A. Grandin, F. Dezitter, M. Weber, J. Strapp, A. Korolev, and C. Williams, 2015: High ice water content at low radar reflectivity near deep convection – Part 1: Consistency of in situ and remote-sensing observations with stratiform rain column simulations. *Atmos. Chem. Phys.*, **15,** 11713–11728. https://doi.org/10.5194/acp-15-11713-2015.

Fritz, S., and I. Laszlo, 1993: Detection of water vapor in the stratosphere over very high clouds in the tropics. *J. Geophys. Res.*, **98,** 22959–22967, https://doi.org/10.1029/93JD01617.

Gage K S, Williams C R, Ecklund W L, and P. E. Johnstonb, 1999: Development and application of Doppler radar profilers to ground validation of satellite precipitation measurements. *Adv. in Space Res.*, **24,** 931-934, https://doi.org/10.1016/S0273-1177(99)00366-X.

Gonzalez, R. C., Eddins, S. L., and Woods, R. E., 2004: *Digital image publishing using MATLAB*. Prentice Hall.

Grandin, A., J. M. Merle, M. Weber, J. Strapp, A. Protat, and P. King, 2014: AIRBUS flight tests in high total water content regions. Proc. *Sixth AIAA Atmospheric and Space Environments Conf.*, Atlanta, GA, American Institute of Aeronautics and Astronautics, AIAA-2014-2753. [Available online at http://arc.aiaa.org/doi/abs/10.2514/6.2014-2753.]

Halverson, J., and Coauthors, 2007: Nasa's Tropical Cloud Systems and Processes Experiment: Investigating Tropical Cyclogenesis and Hurricane Intensity Change. *Bull. Amer. Meteor. Soc.*, **88**, 867–882, https://doi.org/10.1175/BAMS-88-6-867.

Hartmann, J., Gehrmann, M., Kohnert, K., Metzger, S., and Sachs, T., 2018: New calibration procedures for airborne turbulence measurements and accuracy of the methane fluxes during the AirMeth campaigns, *Atmos. Meas. Tech.,* **11,** 4567–4581, https://doi.org/10.5194/amt-11-4567-2018.

Heymsfield, A. J., and J. L. Parrish, 1978: A Computational Technique for Increasing the Effective Sampling Volume of the PMS Two-Dimensional Particle Size Spectrometer. *J. Appl. Meteor.*, **17,** 1566–1572, https://doi.org/10.1175/1520-0450(1978)017<1566:ACTFIT>2.0.CO;2.

Heymsfield, A.J., A. Bansemer, P.R. Field, S.L. Durden, J.L. Stith, J.E. Dye, W. Hall, and C.A. Grainger, 2002: Observations and Parameterizations of Particle Size Distributions in Deep Tropical Cirrus and Stratiform Precipitating Clouds: Results from In Situ Observations in TRMM Field Campaigns. *J. Atmos.Sci*., **59,** 3457–3491. https://doi.org/10.1175/1520-0469(2002)059<3457:OAPOPS>2.0.CO;2.

Heymsfield, A. J., and McFarquhar, G. M., 2002: Mid-latitude and tropical cirrus:

Microphysical properties. *In Cirrus. Oxford University Press*. DOI:10.1093/oso/9780195130720.003.0008.

Heymsfield, A. J., Bansemer, A., Schmitt, C., Twohy, C., and Poellot, M. R., 2004: Effective Ice Particle Densities Derived from Aircraft Data. *J. Atmos. Sci.*, **61,** 982-1003, https://doi.org/10.1175/1520-0469(2004)061<0982:EIPDDF>2.0.CO;2.

Heymsfield, A. J., A. Bansemer, G. M. Heymsfield, and A. O. Fierro, 2009: Microphysics of maritime tropical convective updrafts at temperatures from -20° to -60°C. *J. Atmos. Sci.*, **66,** 3530-3562. https://doi.org/10.1175/2009JAS3107.1.

Heymsfield, A. J., Schmitt, C., Bansemer, A., and Twohy, C. H., 2010: Improved Representation of Ice Particle Masses Based on Observations in Natural Clouds. *J. Atmos. Sci.*, **67,** 3303-3318, https://doi.org/10.1175/2010JAS3507.1.

Heymsfield, A. J., C. Schmitt, and A. Bansemer, 2013: Ice cloud particle size distributions and pressure-dependent terminal velocities from in situ observations at temperatures from 0° to -86°C, *J. Atmos. Sci.*, **70,** 4123–4154, https://doi:10.1175/JAS-D-12-0124.1.

Hodges K., and C. Thorncroft, 1997: Distribution and statistics of the African mesoscale convective systems based on the ISCCP Meteosat Imagery, *Mon. Wea. Rev.*, **125,** 2821-2837, https://doi.org/10.1175/1520-0493(1997)125<2821:DASOAM>2.0.CO;2.

Houze Jr, R. A., 2004: Mesoscale convective systems. *Rev. Geophys.*, **42.** https://doi.org/10.1029/2004RG000150.

Houze Jr, R. A., 2014: Cloud dynamics. *Academic press*. [Available online at https://books.google.com/books?id=GXEpAgAAQBAJ&lpg=PP1&ots=jBaQZYtDYT&dq=Cloud%20Dynamics&lr&hl=zh-CN&pg=PP1#v=onepage&q=Cloud%20Dynamics&f=false.]

Houze Jr, R. A., Wang, J., Fan, J., Brodzik, S., and Feng, Z., 2019: Extreme convective storms over high-latitude continental areas where maximum warming is occurring. *Geophys. Res.Lett.*, **46,** 4059-4065, https://doi.org/10.1029/2019GL082414.

Huang, Y., Wu, W., McFarquhar, G. M., Wang, X., Morrison, H., Ryzhkov, A., Hu, Y., Wolde, M., Nguyen, C., Schwarzenboeck, A., Milbrandt, J., Korolev, A. V., and Heckman, I., 2021: Microphysical Processes Producing High Ice Water Contents (HIWCs) in Tropical Convective Clouds during the HAIC-HIWC Field Campaign: Evaluation of Simulations Using Bulk Microphysical Schemes, *Atmos. Chem. Phys.*, **21,** 6919–6944, https://doi.org/10.5194/acp-21-6919-2021.

Intergovernmental Panel on Climate Change., 2013: Working Group I contribution to the Fifth assessment report of the Intergovernmental Panel on Climate Change. *climate change 2013: The physical science basis. Cambridge University Press*, Cambridge, United Kingdom and New York, NY, USA, 1535 pp. [Available online at https://www.ipcc.ch/report/ar5/wg1/.]

Jackson, R. C., McFarquhar, G. M., Fridlind, A. M., and Atlas, R., 2015: The dependence of cirrus gamma size distributions expressed as volumes in N0-λ-μ phase space and bulk cloud properties on environmental conditions: Results from the Small Ice Particles in Cirrus Experiment (SPARTICUS), *J. Geophys. Res. Atmos.*, **120,** 10351–10377, https://doi.org/10.1002/2015JD023492.

Jakob, C., and S. A. Klein, 1999: The role of vertically varying cloud fraction in the parametrization of microphysical processes in the ECMWF model, Q. *J. R. Meteorol. Soc.*, **125,** 941–965, https://doi.org/10.1002/qj.49712555510.

Jensen, E. J., Lawson, P., Baker, B., Pilson, B., Mo, Q., Heymsfield, A. J., Bansemer, A., Bui, T. P., McGill, M., Hlavka, D., Heymsfield, G., Platnick, S., Arnold, G. T., and Tanelli, S., 2009: On the importance of small ice crystals in tropical anvil cirrus, *Atmos. Chem. Phys.*, **9,** 5519–5537, https://doi.org/10.5194/acp-9-5519-2009.

Jorgensen, D. P., Zipser, E. J., and LeMone, M. A., 1985: Vertical motions in intense hurricanes. *J. Atmos. Sci.*, **42,** 839-856. https://doi.org/10.1175/1520-0469(1985)042<0839:VMIIH>2.0.CO;2.

Kakar, R., Goodman, M., Hood, R., and Guillory, A., 2006: Overview of the Convection and Moisture Experiment (CAMEX). *J. Atmos. Sci.*, **63,** 5-18, https://doi.org/10.1175/JAS3607.1.

Kolios, S., and Feidas, H., 2010: A warm season climatology of mesoscale convective systems in the Mediterranean basin using satellite data. *Theoretical and applied climatology*, **102,** 29-42. https://doi.org/10.1007/s00704-009-0241-7.

Korolev, A. V., Strapp, J. W., Isaac, G. A., and Nevzorov, A. N., 1998: The Nevzorov airborne hot-wire LWC–TWC probe: Principle of operation and performance characteristics. *J. Atmos. Oceanic Technol.*, **15,** 1495-1510, https://doi.org/10.1175/1520-0426(1998)015<1495:TNAHWL>2.0.CO;2.

Korolev, A., 2007: Limitations of the Wegener–Bergeron–Findeisen mechanism in the evolution of mixed-phase clouds. *J. Atmos. Sci.*, **64,** 3372-3375, https://doi.org/10.1175/JAS4035.1.

Korolev, A. V., Emery, E. F., Strapp, J. W., Cober, S. G., Isaac, G. A., Wasey, M., and

Marcotte, D., 2011: Small ice particles in tropospheric clouds: Fact or artifact? Airborne Icing Instrumentation Evaluation Experiment. *B. Am. Meteorol. Soc.*, **92,** 967-973, https://www.jstor.org/stable/26218567.

Korolev, A., Emery, E., and Creelman, K., 2013a: Modification and tests of particle probe tips to mitigate effects of ice shattering. *J. Atmos. Oceanic Tech.*, **30,** 690-708, https://doi.org/10.1175/JTECH-D-12-00142.1.

Korolev, A. V., Emery, E. F., Strapp, J. W., Cober, S. G., and Isaac, G. A., 2013b: Quantification of the effects of shattering on airborne ice particle measurements. *J. Atmos. Oceanic Technol.*, **30,** 2527-2553, https://doi.org/10.1175/JTECH-D-13-00115.1.

Korolev, A. and Field P. R., 2015: Assessment of performance of the inter-arrival time algorithm to identify ice shattering artifacts in cloud particle probes measurements. *Atmosph. Meas. and Techn.*, **8,** 761–777, https://doi.org/10.5194/amt-8-761-2015.

Korolev, A., Heckman, I., and Wolde, M., 2018: Observation of Phase Composition and Humidity in Oceanic Mesoscale Convective Systems, *15th AMS Cloud Physics Conference,* Vancouver, BC. [available online at https://ams.confex.com/ams/15CLOUD15ATRAD/webprogram/Paper347111.html]

Korolev, A., Heckman, I., Wolde, M., Ackerman, A. S., Fridlind, A. M., Ladino, L. A., Lawson, R. P., Milbrandt, J., and Williams, E., 2020: A new look at the environmental conditions favorable to secondary ice production, *Atmos. Chem. Phys.*, **20,** 1391–1429, https://doi.org/10.5194/acp-20-1391-2020.

Krämer, M., Schiller, C., Afchine, A., Bauer, R., Gensch, I., Mangold, A., Schlicht, S., Spelten, N., Sitnikov, N., Borrmann, S., de Reus, M., and Spichtinger, P., 2009: Ice supersaturations and cirrus cloud crystal numbers, *Atmos. Chem. Phys.*, **9,** 3505–3522, https://doi.org/10.5194/acp-9-3505-2009.

Lance, S., C. A. Brock, D. Rogers, and J. A. Gordon, 2010: Water droplet calibration of the Cloud Droplet Probe (CDP) and in-flight performance in liquid, ice and mixed-phase clouds during ARCPAC. *Atmos. Meas. Tech.*, **3,** 1683–1706, https://doi.org/10.5194/amt-3-1683-2010.

Laurent, H., L. Machado, C. Morales, and L. Durieux, 2002: Characteristics of the Amazonian mesoscale convective systems observed from satellite and radar during the WETAMC/LBA experiment, *J. Geophys. Res. Atmos.*, **107,** 1-14, https://doi.org/10.1029/2001JD000337.

Lawson, R.P., Angus L. J., and Heymsfield A. J., 1998: Cloud particle measurements in thunderstorm anvils and possible weather threat to aviation. *J. Aircr.*, **35,** 113–121. https://doi.org/10.2514/2.2268.

Lawson, D. O'Connor, P. Zmarzly, K. Weaver, B. Baker, Q. Mo, and H. Jonsson, 2006: The 2D-S (stereo) probe: Design and preliminary tests of a new airborne, high-speed, high-resolution particle imaging probe. *J. Atmos. Oceanic Technol.*, **23,** 1462–1477, https://doi.org/10.1175/JTECH1927.1.

Lawson, R. P., E. Jensen, D. L. Mitchell, B. Barker, Q. Mo, and B. Pilson, 2010: Microphysical and radiative properties of tropical clouds investigated in TC4 and NAMMA, *J. Geophys. Res.*, **115,** D00J08, https://doi.org/10.1029/2009JD013017.

Leary, C. A., and R. A. Houze, 1980: The Contribution of Mesoscale Motions to the Mass and Heat Fluxes of an Intense Tropical Convective System. *J. Atmos. Sci.*, **37,** 784–796, https://doi.org/10.1175/1520-0469(1980)037<0784:TCOMMT>2.0.CO;2.

Leroy, D., Coutris, P., Emmanuel, F., Schwarzenboeck, A., Strapp, J. W., Lilie, L. E., Korolev, A., McFarquhar, G., Dezitter. F., and Grandin, A., 2016a: HAIC/HIWC field campaigns-Specific findings on ice crystals characteristics in high ice water content cloud regions. In *8th AIAA Atmospheric and Space Environments Conference* (p. 4056). [Available online at https://doi.org/10.2514/6.2016-4056.]

Leroy, D., E. Fontaine, A. Schwarzenboeck, and J. W. Strapp, 2016b: Ice crystal sizes in high ice water content clouds. Part I: On the computation of median mass diameters from in situ measurements. *J. Atmos. Oceanic Technol.*, **33,** 2461–2476, https://doi.org/10.1175/JTECH-D-15-0246.1.

Leroy, D., E. Fontaine, A. Schwarzenboeck, J.W. Strapp, A. Korolev, G. McFarquhar, R. Dupuy, C. Gourbeyre, L. Lilie, A. Protat, J. Delanoë, F. Dezitter, and A. Grandin, 2017: Ice crystal sizes in high ice water content clouds. Part II: Median Mass Diameter Statistics in Tropical Convection observed during the HAIC/HIWC project, *J. Atmos. Ocean. Tech.*, **34,** 117-136. https://doi.org/10.1175/JTECH-D-15-0246.1.

Levizzani, V., and M. Setvák, 1996: Multispectral, high-resolution satellite observations of plumes on top of convective storms. *J. Atmos. Sci.*, **53,** 361–369, https://doi.org/10.1175/1520-0469(1996)053<0361:MHRSOO>2.0.CO;2.

Lilly, D. K., 1988: Cirrus Outflow Dynamics. *J. Atmos. Sci.*, **45,** 1594–1605, https://doi.org/10.1175/1520-0469(1988)045<1594:COD>2.0.CO;2.

Lucas, C., E. J. Zipser, and M. A. Lemone, 1994: Vertical velocity in oceanic convection off tropical Australia. *J. Atmos. Sci.*, **51,** 3183–3193, https://doi.org/10.1175/1520-0469(1994)051<3183:VVIOCO>2.0.CO;2.

Machado, L. A. T., W. B. Rossow, R. L. Guedes, and A. W. Walker, 1998: Life cycle variations of mesoscale convective systems over the Americas, *Mon. Wea. Rev.*, **126,** 1630-1654, https://doi.org/10.1175/1520-0493(1998)126<1630:LCVOMC>2.0.CO;2.

Markowski, P., and Y. Richardson, 2010: Mesoscale Meteorology in Midlatitudes. Wiley, 430 pp.

Mascio, J., McFarquhar, G. M., Hsieh, T., Freer, M., Dooley, A., and Heymsfield, A. J., 2020: The use of gamma distributions to quantify the dependence of cloud particle size distributions in hurricanes on cloud and environmental conditions. *Quart. J. Roy. Meteor. Soc.*, **146,** 2116-2137, https://doi.org/10.1002/qj.3782.

Mason, J., W. Strapp, and P. Chow, 2006: The ice particle threat to engines in flight. *Proc. 44th AIAA Aerospace Sciences Meeting and Exhibit, Reno,* NV, American Institute of Aeronautics and Astronautics, AIAA-2006-206. [Available online at https://doi.org/10.2514/6.2006-206.]

Matsui, T., J. Chern, W. Tao, S. Lang, M. Satoh, T. Hashino, and T. Kubota, 2016: On the Land–Ocean Contrast of Tropical Convection and Microphysics Statistics Derived from TRMM Satellite Signals and Global Storm-Resolving Models. *J. Hydrometeor.*, **17,** 1425–1445, https://doi.org/10.1175/JHM-D-15-0111.1.

May, P. T., Mather, J. H., Vaughan, G., Jakob, C., McFarquhar, G. M., Bower, K. N., and Mace, G. G., 2008: The tropical warm pool international cloud experiment, *B. Am. Meteorol. Soc.*, **89,** 629– 646, 2008. https://doi.org/10.1175/BAMS-89-5-629.

Mazin, I. P., Korolev, A. V., Heymsfield, A., Isaac, G. A., and Cober, S. G., 2001: Thermodynamics of icing cylinder for measurements of liquid water content in supercooled clouds. *J. Atmos. Oceanic Technol.*, **18,** 543-558, https://doi.org/10.1175/1520-0426(2001)018<0543:TOICFM>2.0.CO;2.

McFarquhar, G. M., and A. J. Heymsfield, 1996: Microphysical characteristics of three anvils sampled during the Central Equatorial Pacific Experiment. *J. Atmos. Sci.*, **53,** 2401–2423, https://doi.org/10.1175/1520-0469(1996)053<2401:MCOTAS>2.0.CO;2.

McFarquhar, G. M., Heymsfield, A. J., Spinhirne, J., and Hart, B., 2000: Thin and subvisual tropopause tropical cirrus: Observations and radiative impacts. *J. Atmos. Sci.*, **57,** 1841-1853. https://doi.org/10.1175/1520-0469(2000)057<1841:TASTTC>2.0.CO;2.

McFarquhar, G. M., Iacobellis, S., and Somerville, R. C. J., 2003: SCM Simulations of Tropical Ice Clouds Using Observationally Based Parameterizations of Microphysics. *J. Climate.*, **16,** 1643-1664, https://doi.org/10.1175/1520-0442(2003)016<1643:SSOTIC>2.0.CO;2.

McFarquhar G M and Black R A., 2004: Observations of particle size and phase in tropical cyclones: Implications for mesoscale modeling of microphysical processes. *J. Atmos. Sci.*, **61,** 422-439, https://doi.org/10.1175/1520-0469(2004)061<0422:OOPSAP>2.0.CO;2.

McFarquhar, G. M., Um, J., Freer, M., Baumgardner, D., Kok, G. L., and Mace, G., 2007a:

Importance of small ice crystals to cirrus properties: Observations from the Tropical Warm Pool International Cloud Experiment (TWP-ICE). *Geophys. Res. Lett.*, **34,** L13803, https://doi.org/10.1029/2007GL029865.

McFarquhar, G. M., M. S. Timlin, R. M. Rauber, B. F. Jewett, J. A. Grim, and D. P. Jorgensen, 2007b: Vertical Variability of Cloud Hydrometeors in the Stratiform Region of Mesoscale Convective Systems and Bow Echoes. *Mon. Wea. Rev.*, **135,** 3405–3428, https://doi.org/10.1175/MWR3444.1.

McFarquhar, G.M., D. Baumgardner, A. Bansemer, S. Abel, J. Crosier, J. French, P. Rosenberg, A. Korolev, A. Schwarzenboeck, D. Leroy, J. Um, W. Wu, A.J. Heymsfield, A. Detwiler, P. Field, A. Neumann, J. Stith, D. Axisa, R. Cotton, and J. Dong, 2017: Processing of ice cloud in situ data collected by bulk water, scattering and imaging probes: Fundamentals, uncertainties and efforts towards consistency. *Amer. Meteor. Soc. Monographs*, **58,** II.1-11.31, https://doi.org/10.1175/AMSMONOGRAPHS-D-16-0007.1.

Meyers, M. P., DeMott, P. J., and Cotton, W. R., 1992: New primary ice-nucleation parameterizations in an explicit cloud model. *J Appl Meteorol.*, **31,** 708–721, https://doi.org/10.1175/1520-0450(1992)031<0708:NPINPI>2.0.CO;2.

Mitchell, D. L., Rasch, P., Ivanova, D., McFarquhar, G., and Nousiainen, T., 2008: Impact of small ice crystal assumptions on ice sedimentation rates in cirrus clouds and GCM simulations. *Geophys. Res. Lett.*, **35,** L09806, https://doi.org/10.1029/2008GL033552.

Muhlbauer, A., Ackerman, T. P., Comstock, J. M., Diskin, G. S., Evans, S. M., Lawson,

R. P., and Marchand, R. T., 2014: Impact of large-scale dynamics on the microphysical properties of midlatitude cirrus. *J. Geophys. Res. Atmos.*, **119,** 3976-3996, https://doi.org/10.1002/2013JD020035.

Murphy, A.M., R.M. Rauber, G.M. McFarquhar, J.A. Finlon, D.M. Plummer, A.A. Rosenow, and B.F. Jewett, 2017: A microphysical analysis of elevated convection in the comma head region of continental winter cyclones. *J. Atmos. Sci.*, **74**, 69-91, https://doi.org/10.1175/JAS-D-16-0204.1.

Nguyen, C. M., M. Wolde, and A. Korolev, 2019: Determination of ice water content (IWC) in tropical convective clouds from X-band dual-polarization airborne radar. *Atmos. Meas. Tech.*, **12,** 5897–5911, https://doi.org/10.5194/amt-12-5897-2019.

Nieman, S. J., W. P. Menzei, C. M. Hayden, D. Gray, S. T. Wanzong, C. S. Velden, and J. Daniels, 1997: Fully Automated Cloud-Drift Winds in NESDIS Operations. *Bull. Amer. Meteor. Soc.*, **78**, 1121–1134, https://doi.org/10.1175/1520-0477(1997)078<1121:FACDWI>2.0.CO;2.

Protat, A., D. Bouniol, J. Delano, P. T. May, A. Plana-Fattori, A. Hasson, E. O'Connor, U. Görsdorf, and A. J. Heymsfield, 2009: Assessment of Cloudsat Reflectivity Measurements and Ice Cloud Properties Using Ground-Based and Airborne Cloud Radar Observations. *J. Atmos. Oceanic Technol.*, ***26,*** 1717-1741, https://doi.org/10.1175/2009JTECHA1246.1.

Rafati S., and M. Karimi, 2017: Assessment of mesoscale convective systems using IR brightness temperature in the southwest of Iran, *Theor. Appl. Climatol.*, **129,** 539-549, https://doi.org/10.1007/s00704-016-1797-7.

Ratvasky, T.P., Harrah, S. D., Strapp, J. W., Lilie, L.E., Proctor, F.H., Strickland, J. K., Hunt, P. J., Bedka, K. M., Diskins, G. S., Nowak, J. B., Bui, T. V., Bansemer, A., and Dumont, C. J., 2019: Summary of the High Ice Water Content (HIWC) RADAR Flight Campaigns, *SAE Technical Paper*. [Available online at https://doi.org/10.4271/2019-01-2027.]

Sanderson, B. M., C. Piani, W. J. Ingram, D. A. Stone, and M. R. Allen, 2008:, Towards constraining climate sensitivity by linear analysis of feedback patterns in thousands of perturbed-physics GCM simulations, *Clim. Dyn.*, **30,** 175–190. [Available online at https://link.springer.com/content/pdf/10.1007/s00382-007-0280-7.pdf.]

Sobel, A. H., Yuter, S. E., Bretherton, C. S., and Kiladis, G. N., 2004: Large-Scale Meteorology and Deep Convection during TRMM KWAJEX. *Mon. Wea. Rev.*, **132,** 422-444, https://doi.org/10.1175/1520-0493(2004)132<0422:LMADCD>2.0.CO;2.

Stanford, M. W., Varble, A., Zipser, E., Strapp, J. W., Leroy, D., Schwarzenboeck, A., Potts, R., and Protat, A., 2017: A ubiquitous ice size bias in simulations of tropical deep convection. *Atmos. Chem. Phys.*, **17,** 9599-9621, https://doi.org/10.5194/acp-17-9599-2017.

Stephens, G. L., 2005: Cloud feedbacks in the climate system: A critical review, *J. Clim.*, **18,** 237–273, https://doi.org/10.1175/JCLI-3243.1.

Strapp, J. W., J. MacLeod, and L. Lilie, 2008: Calibration of ice water content in a wind tunnel/engine test cell facility. Extended Abstracts, *15th Int. Conf. on Cloud and Precipitation,* Cancun, Mexico, International Commission on Clouds and Precipitation, P13.1. [Available online at http://cabernet. atmosfcu.unam.mx/ICCP-2008/abstracts/Program_on_line/ Poster_13/StrappEtAl-extended.pdf.]

Strapp, J.W., L. E. Lilie, T. P. Ratvasky, C. R. Davison, and C. Dumont, 2016a: Isokinetic TWC Evaporator Probe: Development of the IKP2 and performance testing for the HAIC-HIWC Darwin 2014 and Cayenne Field Campaigns. *Proc. Eighth AIAA Atmospheric and Space Environments Conf.*, Washington, DC, American Institute of Aeronautics and Astronautics, AIAA-2016-4059. [Available online at http://arc.aiaa.org/doi/10.2514/6.2016-4059.]

Strapp, J.W., A. Korolev, T. Ratvasky, R. Potts, A. Protat, P. May, A. Ackerman, A. Fridlind, P. Minnis, J. Haggerty, J. T. Riley, Lyle E. Lilie, and G. A. Isaac, 2016b: The High Ice Water Content (HIWC) study of deep convective clouds: Science and technical plan. *FAA Rep.* DOT/FAA/TC-14/31, 105 pp. [Available online at http://www.tc.faa.gov/its/worldpac/techrpt/tc14-31.pdf.]

Strapp, J. W., Schwarzenboeck, A., Bedka, K. , Bond, T., Calmels, A., Delanoë, J., Dezitter, F., Grzych, M., Harrah, S., Korolev, A., Leroy, D., Lilie, L., Mason, J., Potts, R., Protat, A., Ratvasky, T., Riley, J., and Wolde, M., 2020: An Assessment of Cloud Total Water Content and Particle Size from Flight Test Campaign Measurements in High Ice Water Content, Mixed Phase/Ice Crystal Icing Conditions: Primary In-Situ Measurements, *FAA Rep.* DOT/FAA/TC-18/1. [Available online at http://www.tc.faa.gov/its/worldpac/techrpt/tc18-1.pdf.]

Strapp, J., Schwarzenboeck, A., Bedka, K., Bond, T., Calmels, A., Delanoë, J., Dezitter, F., Grzych, M., Harrah, S., Korolev, A., Leroy, D., Lilie, L., Mason, J., Potts, R., Protat, A., Ratvasky, T., Riley, J., and Wolde, M., 2021: Comparisons of Cloud In Situ Microphysical Properties of Deep Convective Clouds to Appendix D/P Using Data from the High-Altitude Ice Crystals-High Ice Water Content and High Ice

Water Content-RADAR I Flight Campaigns, *SAE Int. J. Aerosp.* 14(2): https://doi.org/10.4271/01-14-02-0007.

Toon, O. B., Starr, D. O., Jensen, E. J., Newman, P. A., Platnick, S., Schoeberl, M. R., Wennberg, P. O., Wofsy, S. C., Kurylo, M. J., Maring, H., Jucks, K. W., Craig, M. S., Vasques, M. F., Pfister, L., Rosenlof, K. H., Selkirk, H. B., Colarco, P. R., Kawa, S. R., Mace, G. G., Minnis, P., and Pickering, K. E., 2010: Planning, implementation, and first results of the Tropical Composition, Cloud and Climate Coupling Experiment (TC4). *J. Geophys. Res. Atmos.*, **115,** D00J04, https://doi.org/10.1029/2009JD013073.

Velden, C. S., C. M. Hayden, S. J. Nieman, W. P. Menzel, S. Wanzong, and J. S. Goerss, 1997: Upper-tropospheric winds derived from geostationary satellite water vapor observations. *Bull. Amer. Meteor. Soc.*, **78,** 173–195, https://doi.org/10.1175/1520-0477(1997)078<0173:UTWDFG>2.0.CO;2.

Vila, D. A., L. A. T. Machado, H. Laurent, and I. Velasco, 2008: Forecast and tracking the evolution of cloud clusters (fortracc) using satellite infrared imagery: methodology and validation, *Wea. Forecasting*, **23,** 233-245, https://doi.org/10.1175/2007WAF2006121.1.

Wolde, M., and Pazmany A., 2005: NRC dual-frequency airborne radar for atmospheric research. *32nd Conf. on Radar Meteorology*, Albuquerque, NM, Amer. Meteor. Soc., P1R.9. [Available online at https://ams.confex.com/ams/32Rad11Meso/techprogram/paper_96918.htm.]

Wolde, M., Nguyen, C., Korolev, A., and Bastian, M., 2016: Characterization of the Pilot

X-band radar responses to the HIWC environment during the Cayenne HAIC-HIWC 2015 Campaign. In *8th AIAA Atmospheric and Space Environments Conference* (p. 4201). [Available online at https://doi.org/10.2514/6.2016-4201.]

Wu, Q., H. Wang, Y. Lin, Y. Zhuang, and Y. Zhang, 2016: Deriving AMVs from Geostationary Satellite Images Using Optical Flow Algorithm Based on Polynomial Expansion. *J. Atmos. Oceanic Technol.*, **33**, 1727–1747, https://doi.org/10.1175/JTECH-D-16-0013.1.

Yost, C. R., Bedka, K. M., Minnis, P., Nguyen, L., Strapp, J. W., Palikonda, R., Khlopenkov, K., Spangenberg, D., Smith Jr., W. L., Protat, A., and Delanoe, J., 2018: A prototype method for diagnosing high ice water content probability using satellite imager data, *Atmos. Meas. Tech.*, **11,** 1615–1637, https://doi.org/10.5194/amt-11-1615-2018.

Zipser, E. J., C. Liu, D. J. Cecil, S. W. Nesbitt, and D. P. Yorty, 2006: Where are the most intense thunderstorms on Earth? *Bull. Amer. Meteor. Soc.*, **87,** 1057–1071, https://doi.org/10.1175/BAMS-87-8-1057.

Table 1. Overview of the 17 flights through 14 MCSs during the HAIC-HIWC Cayenne campaign. Peak *IWC* values derived from IKP2 measurements at 5-second resolution. A double bar indicates there are no data at this temperature level.

Flight number (date, time period)	Maximum *IWCs* at different flight levels (g/m^3)			Underlying surface	UTC (date) hh:mm (dd/mm)		Life cycle (hour)
	-15 to -5 ^{o}C	-35 to -25 ^{o}C	-50 to -40 ^{o}C		Initial time	Dissipation time	
F10 (10/05, 19:03-21:21)	--	--	2.1	Continental	18:15 (10/05)	00:45 (11/05)	6.5
F11 (12/05, 20:20-22:26)	--	1.3	0.7	Continental	17:15 (12/05)	11:15 (13/05)	18
F12 (14/05, 14:17-17:15)	--	0.4	--	Coastal	07:15 (14/05)	19:15 (14/05)	12
F13 (15/05, 08:35-12:09)	3.9	3.1	2.1	Oceanic	02:15 (15/05)	21:15 (15/05)	19
F14 (16/05, 08:23-11:54)	1.0	3.3	--	Oceanic	01:45 (16/05)	19:15 (17/05)	41.5
F15 (16/05, 15:59-18:33)	2.9	2.1	--	Continental			
F16 (18/05, 19:27-22:20)	2.2	2.5	1.5	Oceanic	03:45 (18/05)	02:15 (19/05)	22.5
F17 (19/05, 14:19-17:27)	--	2.3	1.9	Oceanic	01:45 (19/05)	22:15 (20/05)	44.5
F18 (23/05, 09:14-12:44)	--	2.6	--	Oceanic	02:45 (23/05)	22:45 (23/05)	20
F19 (23/05, 15:23-18:59)	3.1	1.8	2.3	Oceanic			
F20 (24/05, 08:51-12:08)	3.6	3.2	2.7	Oceanic	22:45 (23/05)	15:45 (24/05)	17
F21 (25/05, 19:07-22:40)	--	2.6	2.6	Continental	14:45 (25/05)	14:15 (26/05)	23.5
F22 (26/05, 08:33-11:59)	3.7	3.1	3.5	Oceanic	21:15 (25/05)	06:15 (27/05)	33
F23 (26/05, 13:10-15:51)	3.2	1.4	2.4	Oceanic			
F24 (27/05, 08:27-12:06)	3.0	3.4	--	Oceanic	05:15 (27/05)	23:45 (27/05)	18.5
F25 (28/05, 19:25-22:53)	2.3	1.9	1.5	Continental	12:15 (28/05)	07:15 (29/05)	19
F26 (29/05, 08:47-12:06)	3.1	2.6	3.0	Coastal	22:45 (28/05)	21:15 (29/05)	22.5

Table 2. Number of 5-second samples acquired in different environmental conditions

MCS types	**Flight Temperature levels**			**Total**
	-15 to -5 °C	**-35 to -25 °C**	**-50 to -40 °C**	
Oceanic	2619	3041	1751	7411
Coastal	290	352	904	1546
Continental	450	989	1943	3382
Vertical motions	**Flight Temperature levels**			**Total**
	-15 to -5 °C	**-35 to -25 °C**	**-50 to -40 °C**	
Updrafts	146	249	214	609
stratiform	3181	4024	4115	11320
Downdrafts	32	109	269	410
MCS age	**Flight Temperature levels**			**Total**
	-15 to -5 °C	**-35 to -25 °C**	**-50 to -40 °C**	
< 6h	120	733	1196	2049
6 – 12h	1173	2294	1334	4801
> 12h	2066	1355	2068	5489
Distance from convective core (km)	**Flight Temperature levels**			**Total**
	-15 to -5 °C	**-35 to -25 °C**	**-50 to -40 °C**	
≤ 50	902	1493	1293	3688
50-100	548	1064	1021	2633
100-200	942	989	1434	3365
>200	967	836	850	2653
$BTD_{6.8-10.8\mu m}$	**Flight Temperature levels**			**Total**
	-15 to -5 °C	**-35 to -25 °C**	**-50 to -40 °C**	
< -3K	302	861	535	1698
-3 to -1K	1478	2474	2072	6024
> -1K	1579	1047	1991	4617
Total	3359	4382	4598	12339

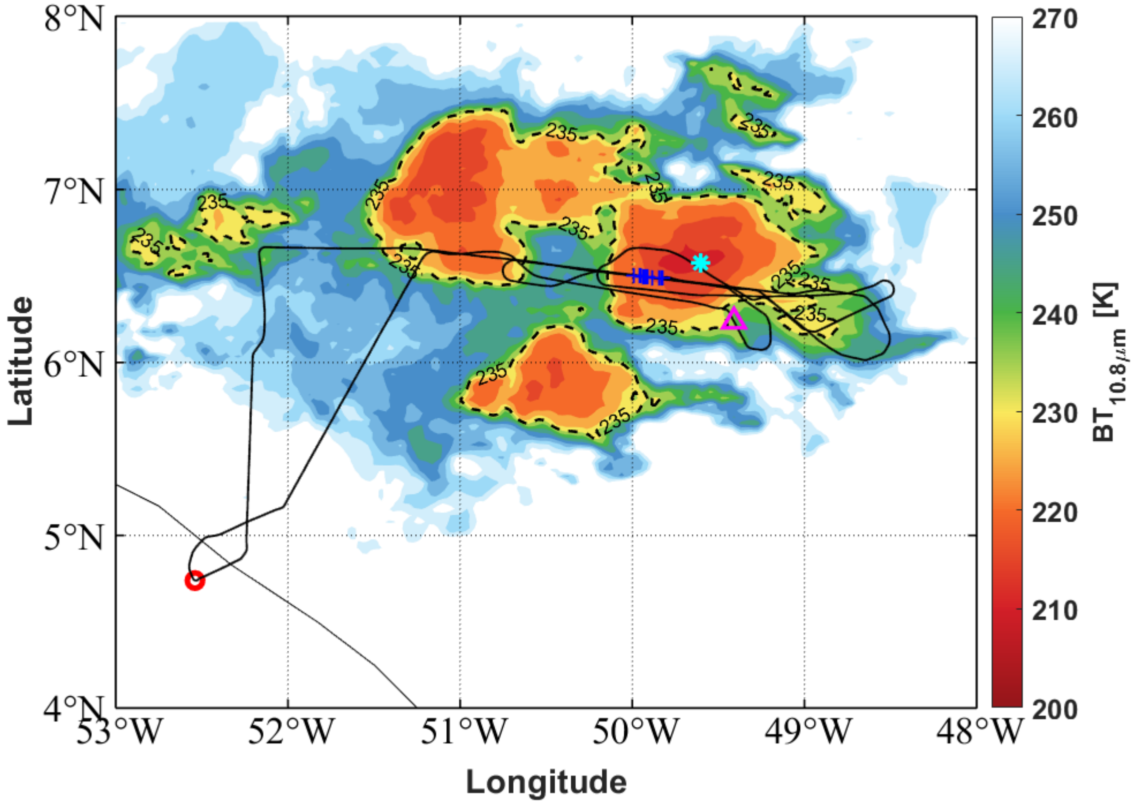

Figure 1. GOES-13 measured brightness temperature ($BT_{10.8\mu m}$) at 15 May 2015 11:15:00 UTC with flight track of Falcon 20 overlaid with black line for Flight 13. The black dashed line shows the temperature contour line at 235K. Red circle indicates location of Cayenne (52.5 °W, 4.74 °N), blue points indicate where IKP2 $IWC > 1.5$ g m^{-3} and $MMD < 400$ µm between -50 °C ≤ T ≤ -40 °C, magenta triangle and cyan asterisk ($BT_{10.8\mu m}$ = 213.6 K) denote location of aircraft and of MCS convective core at 11:15:00 UTC, respectively.

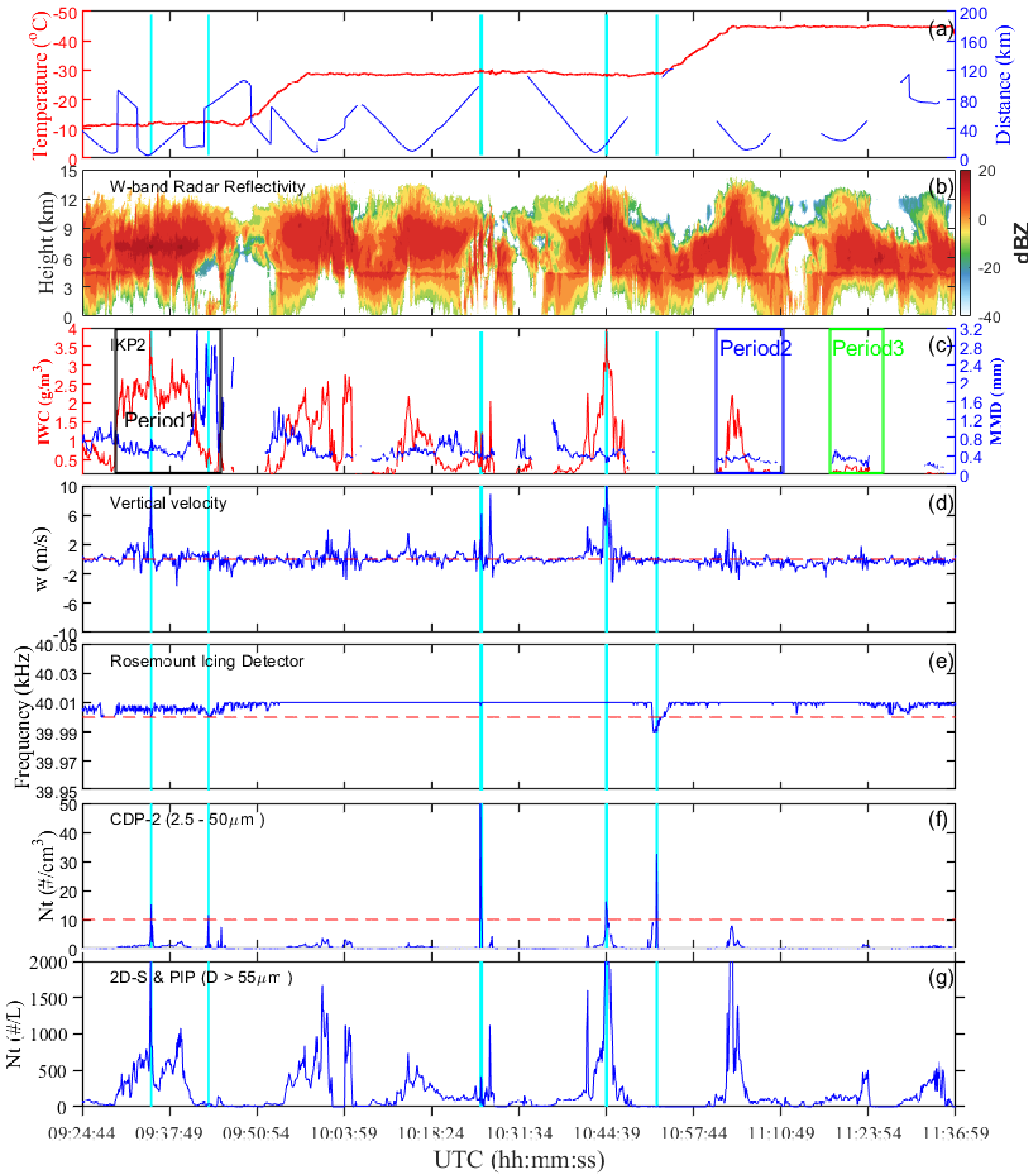

Figure 2. Time series of (a) temperature at flight altitude (red line), distance away from convective core (blue line, times when aircraft flew out of MCS not shown); (b) W-band radar reflectivity from the multi-beam 95GHz Doppler cloud radar mounted on Falcon 20; (c) *IWC* from IKP2 (red line) and *MMD* (blue line); (d) vertical velocity (*w*); (e) Rosemount

icing detector frequency (blue line) with threshold of 40 kHz indicating presence of supercooled liquid water (red line); (f) total number concentration (N_t) with diameter between 2.5 and 50 μm measured by CDP-2 (blue line) and threshold of 10 cm^{-3} corresponding to liquid water (red line) and (g) N_t from composite 2D-S (D_{max} > 55 μm) and PIP size distribution for 09:24:44 - 11:36:59 UTC 15 May 2015 flight leg. Shaded gray boxes represent locations of Rosemount icing detector frequency less than 40 kHz, shaded cyan boxes indicated N_t measured by CDP-2 larger than 10 cm^{-3}.

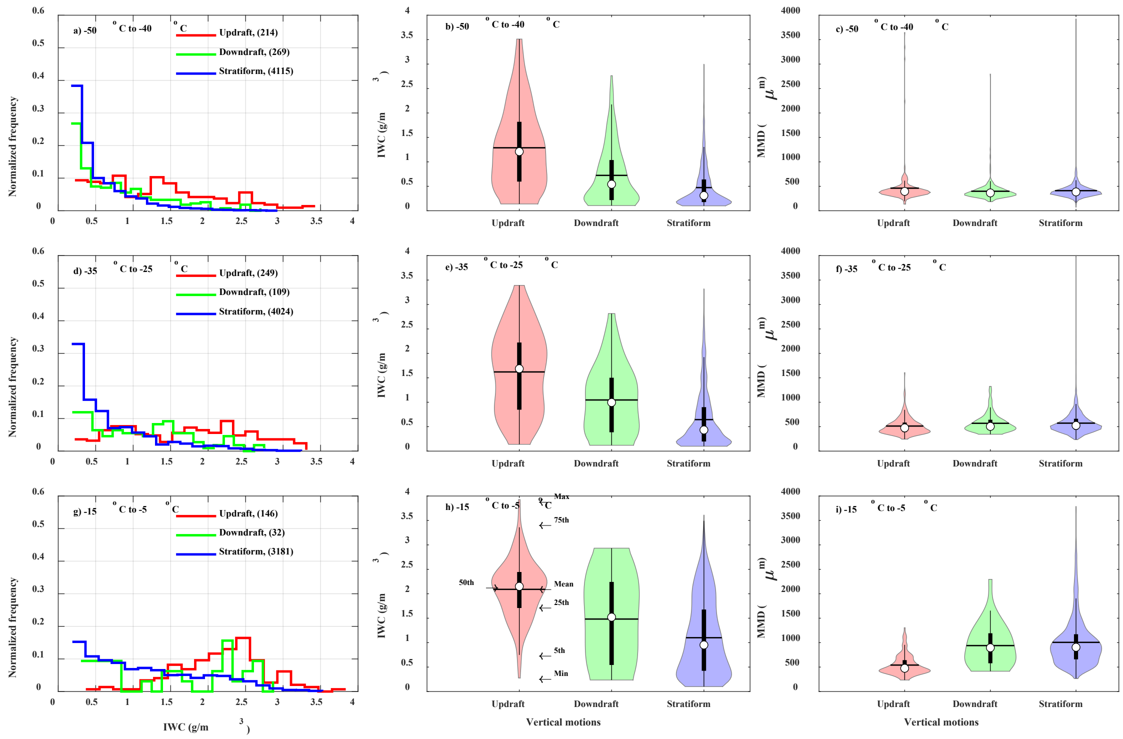

Figure 3. Normalized frequency of occurrence of *IWC* for updrafts, downdrafts and stratiform regions for temperature levels: (a) -50 ºC to -40 ºC, (d) -35 ºC to -25 ºC and (g) -15 ºC to -5 ºC. Red represents updrafts, green downdrafts, and blue stratiform regions. Number of data points for each condition shown in legend. (b, e, and h). Violin plots of *IWC* for updrafts, downdrafts and stratiform regions for each *T*. Top and bottom of the

violin plot indicate maximum and minimum, respectively. Black boxplots, show 5th, 25th, 50th (white point), 75th, and 95th percentile of distribution. Horizontal black line indicates mean value. Width of shaded area represents proportion of data located there. (c, f, and i) As (a, d, and g) but for *MMD*.

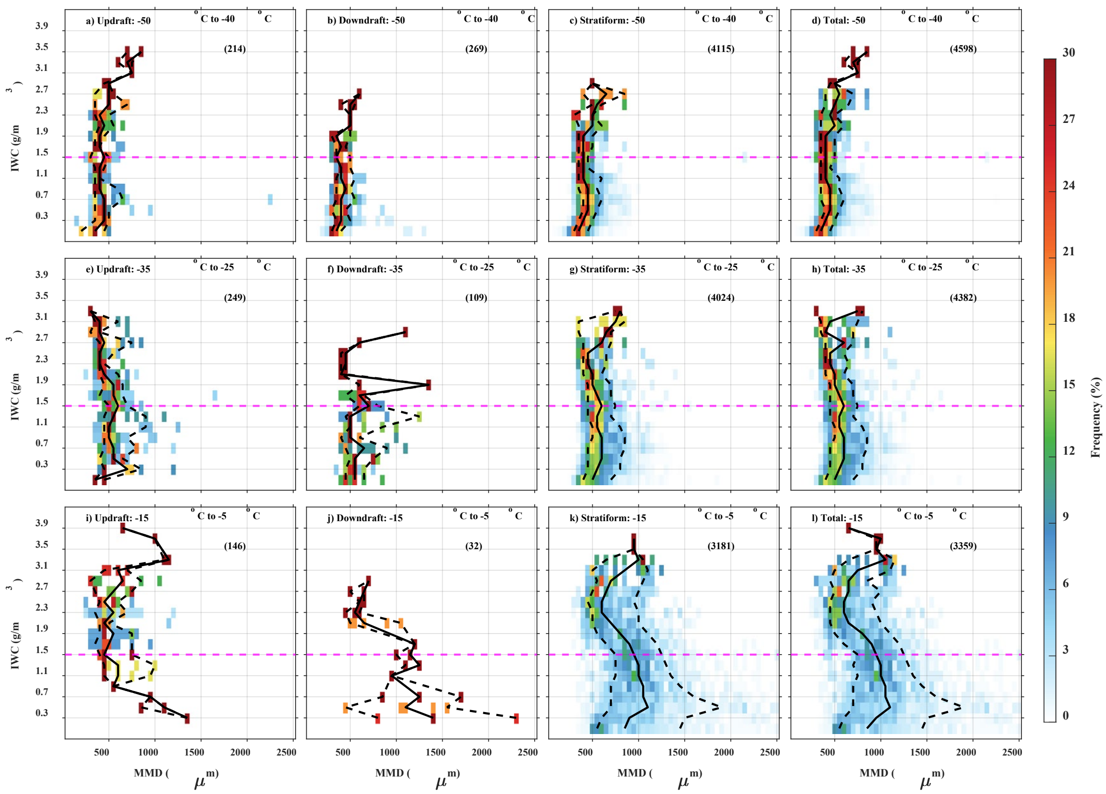

Figure 4. Normalized frequency of *MMD* for each *IWC* range for (a) updrafts, (b) downdrafts, (c) stratiform regions, and (d) all three combined for temperatures between -50 °C and -40 °C. (e-h) As in figures 4a-4d but for temperatures -35 °C to -25 °C. (i-l) As in figures 4a-4d but for temperatures -15 °C to -5 °C. For each subplot, the middle solid line indicates the 50th percentile, whereas the left and right dash lines represent 15th and 85th *MMD* respectively. The magenta dashed horizontal lines mean *IWC* = 1.5 g m^{-3}. Numbers in brackets give number of sample data points.

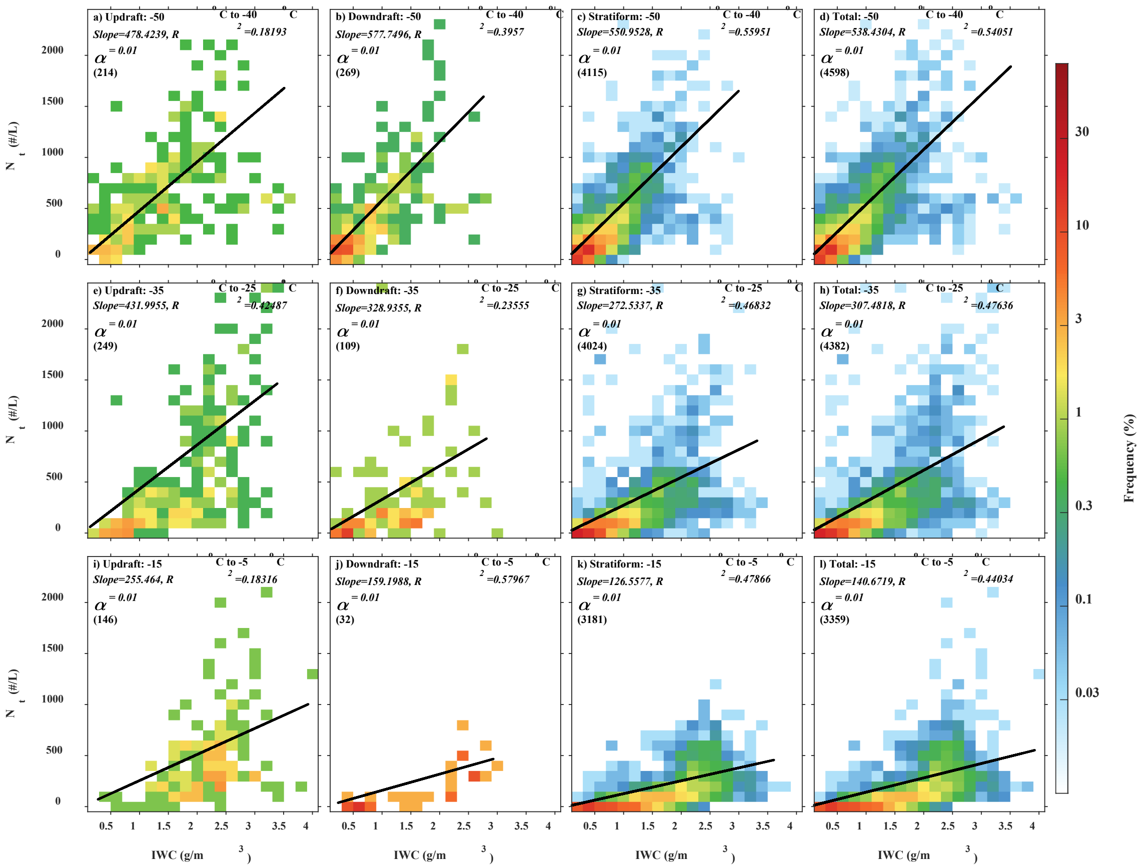

Figure 5. Normalized 2-dimensional frequency distributions of N_t and *IWC* for (a) updrafts, (b) downdrafts, (c) stratiform regions, and (d) all three combined for temperatures from -50 ºC to -40 ºC. (e-h) As in figures 5a-5d but for temperatures -35 ºC to -25 ºC. (i-l) As in figures 5a-5d but for temperatures -15 ºC to -5 ºC. For each subplot, black line gives best fit. Slope of fit line, coefficient of determination R^2, and significance level (α) are shown. Numbers in brackets represent number of sample data points.

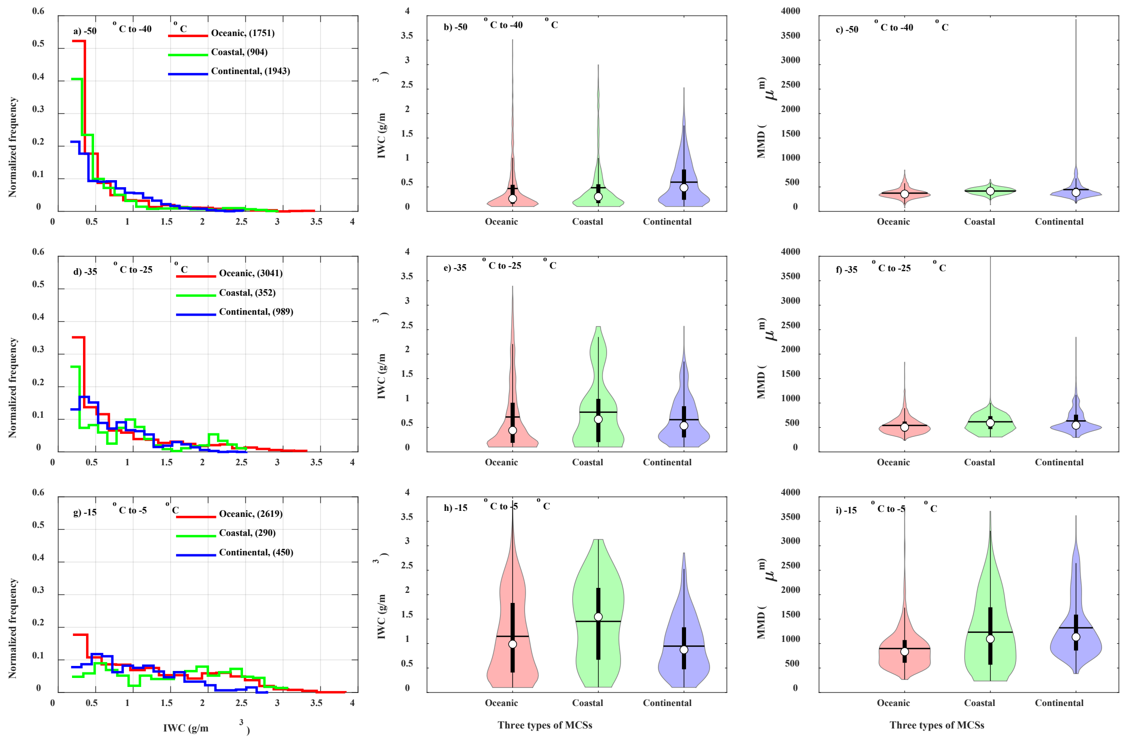

Figure 6. As in figure 3 but for MCSs over different surfaces (oceanic, coastal, and continental) rather than for updrafts, downdrafts and stratiform regions.

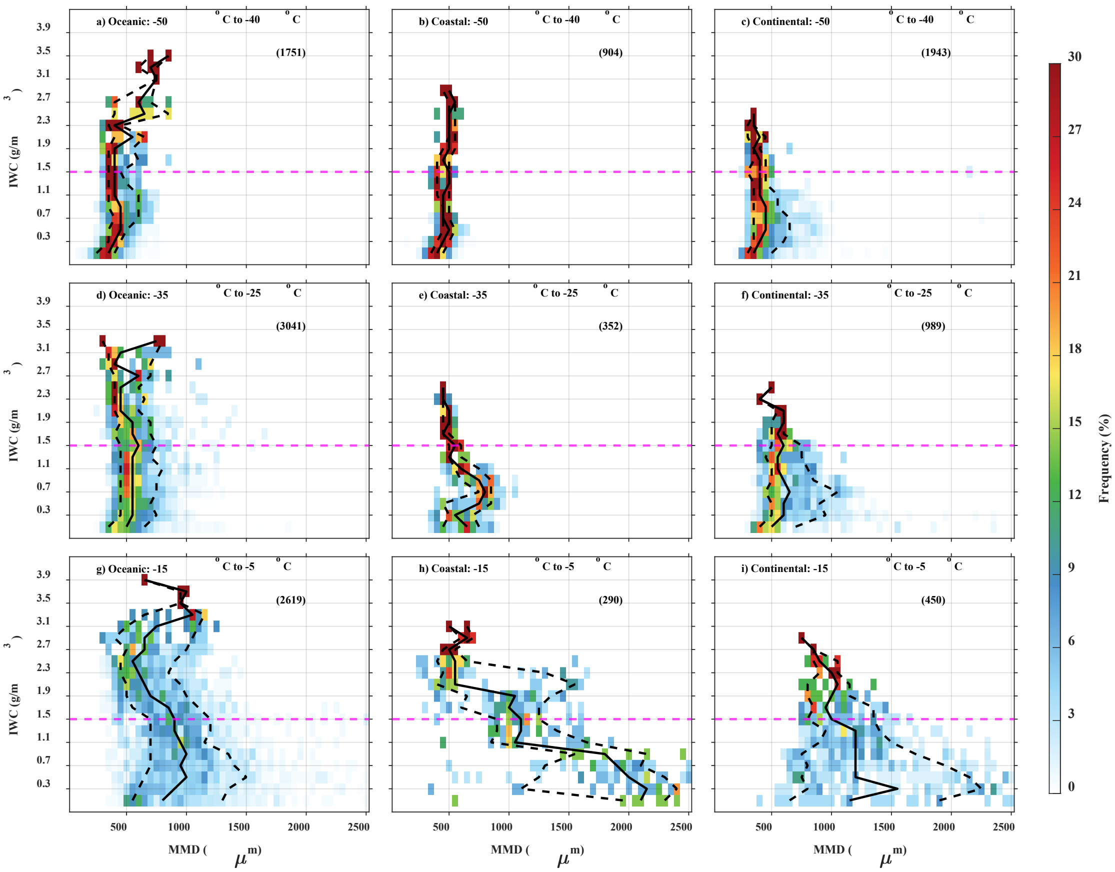

Figure 7. As in figure 4 but for MCSs over different surfaces (oceanic, coastal, and continental) rather than for updrafts, downdrafts and stratiform regions.

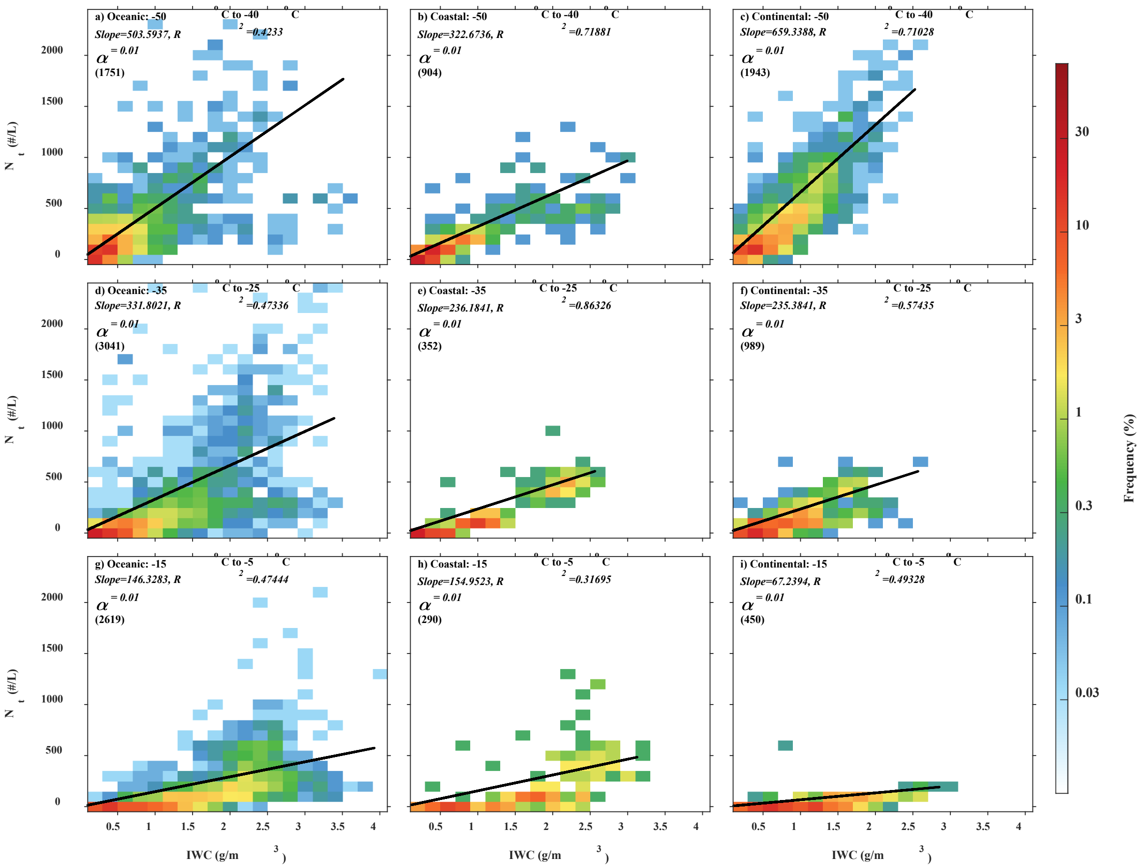

Figure 8. As in figure 5 but for MCSs over different surfaces (oceanic, coastal, and continental) rather than for updrafts, downdrafts and stratiform regions.

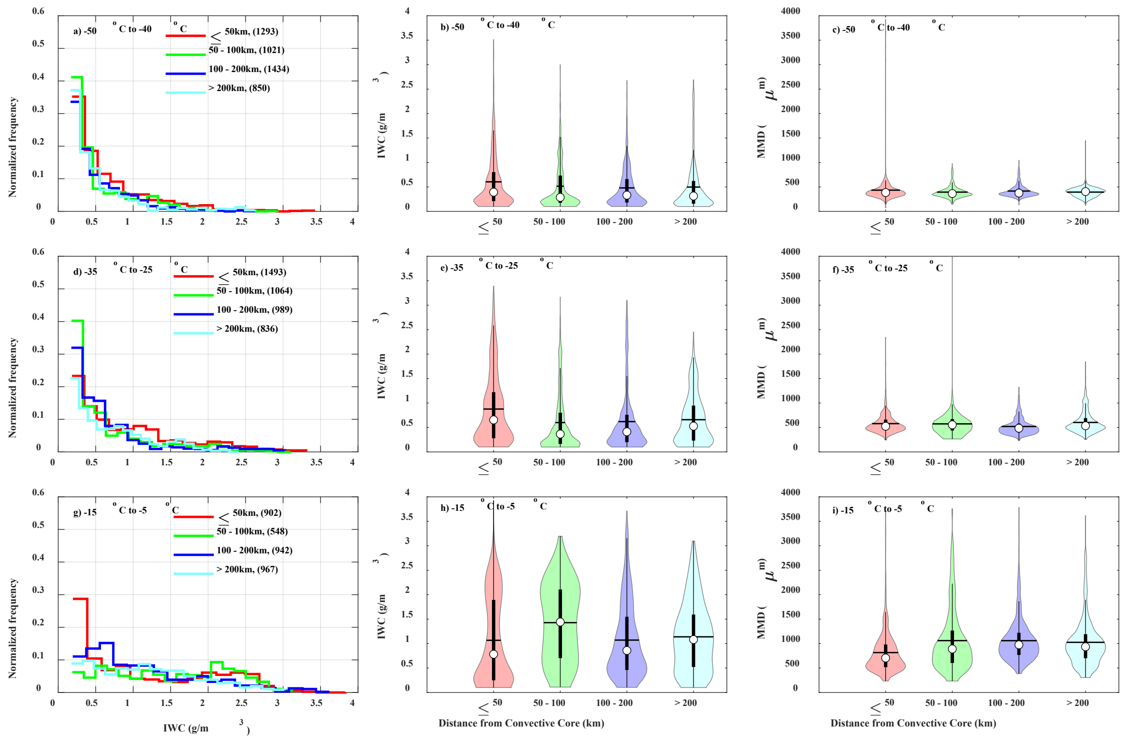

Figure 9. As in figure 3 but for MCSs sorted by distance of measurement from convective core ($L \leq 50$ km, 50 km $< L \leq 100$ km, 100 km $< L \leq 200$ km, $L > 200$ km) rather than for updrafts, downdrafts and stratiform regions.

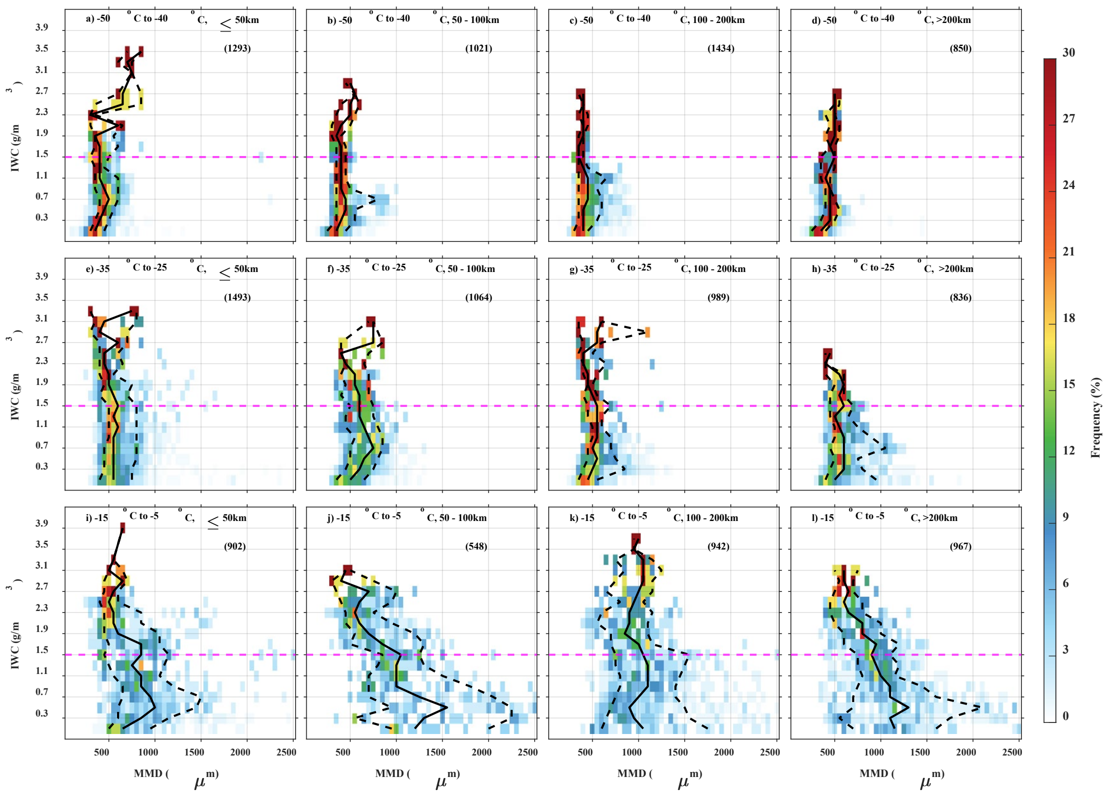

Figure 10. As in figure 4 but for MCSs sorted by distance of measurement from convective core ($L \leq 50$ km, 50 km $< L \leq 100$ km, 100 km $< L \leq 200$ km, $L > 200$ km) rather than for updrafts, downdrafts and stratiform regions.

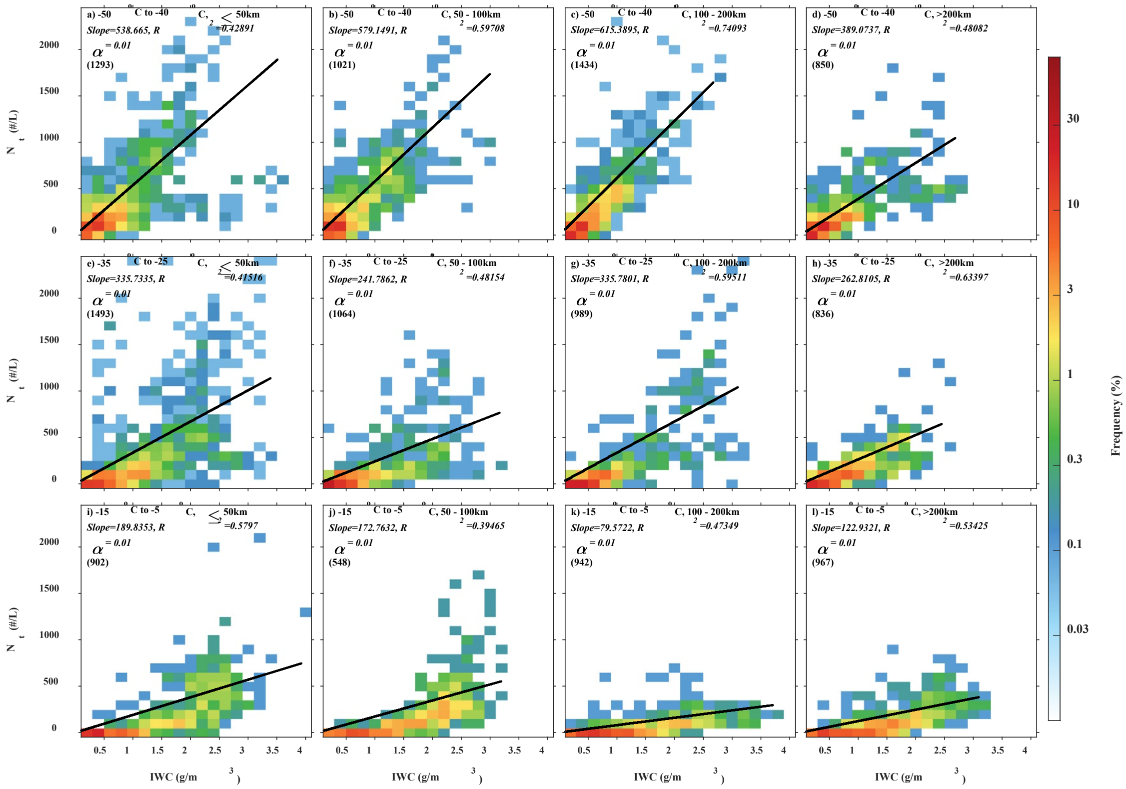

Figure 11. As in figure 5 but for MCSs sorted by distance from convective core ($L \leq 50$ km, 50 km $< L \leq 100$ km, 100 km $< L \leq 200$ km, $L > 200$ km) rather than for updrafts, downdrafts and stratiform regions.

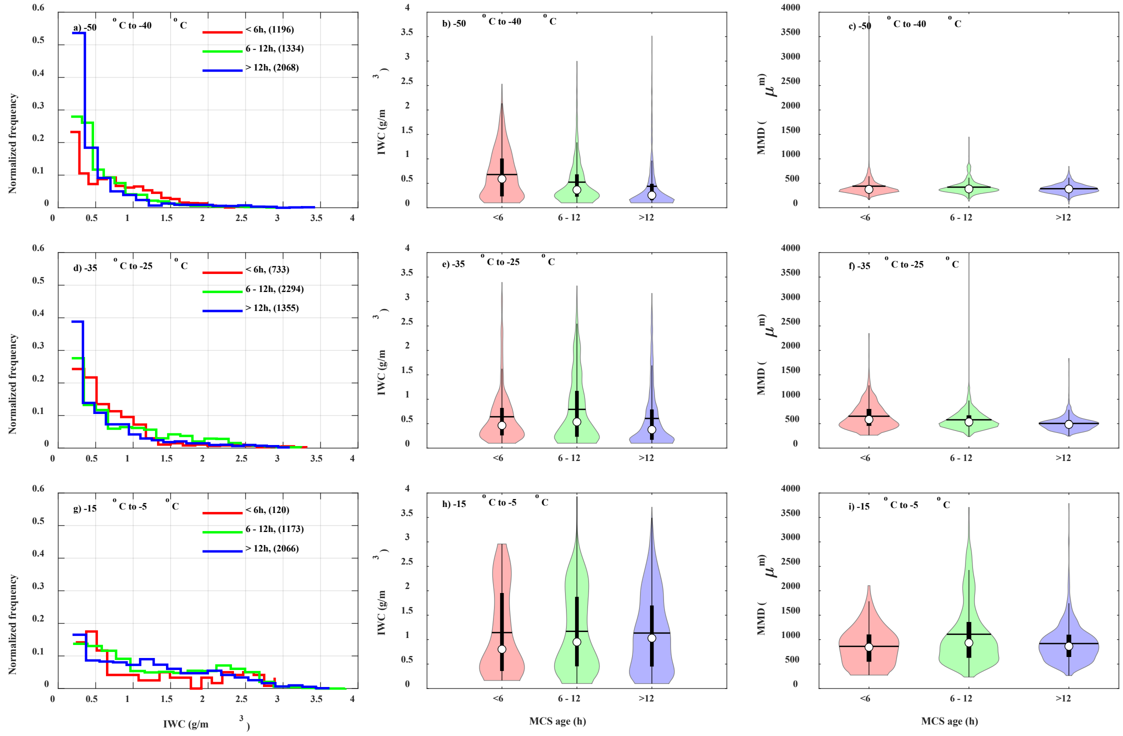

Figure 12. As in figure 3 but for MCSs sorted by age (< 6h, 6-12h and >12h) rather than for updrafts, downdrafts and stratiform regions.

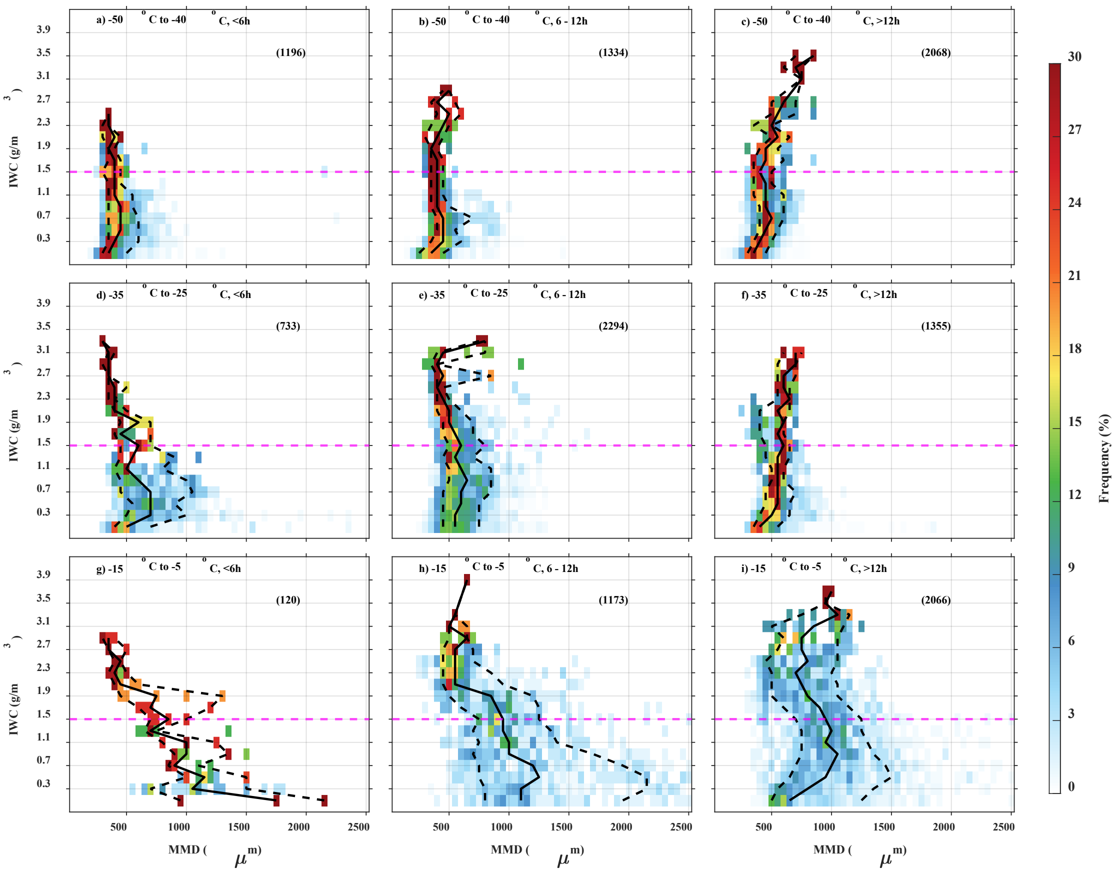

Figure 13. As in figure 4 but for MCSs sorted by age (< 6h, 6-12h and >12h) rather than for updrafts, downdrafts and stratiform regions.

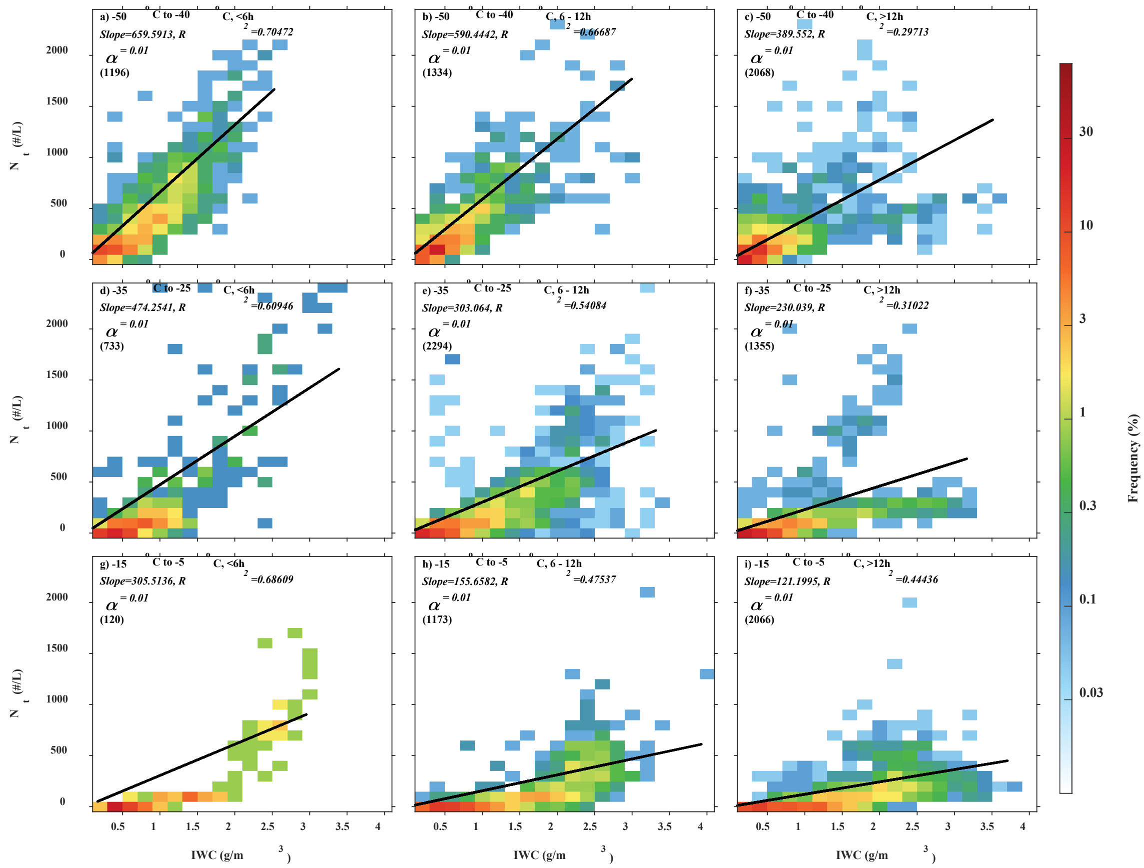

1288

1289 Figure 14. As in figure 5 but for MCSs sorted by age (< 6h, 6-12h and >12h) rather than

1290 for updrafts, downdrafts and stratiform regions.

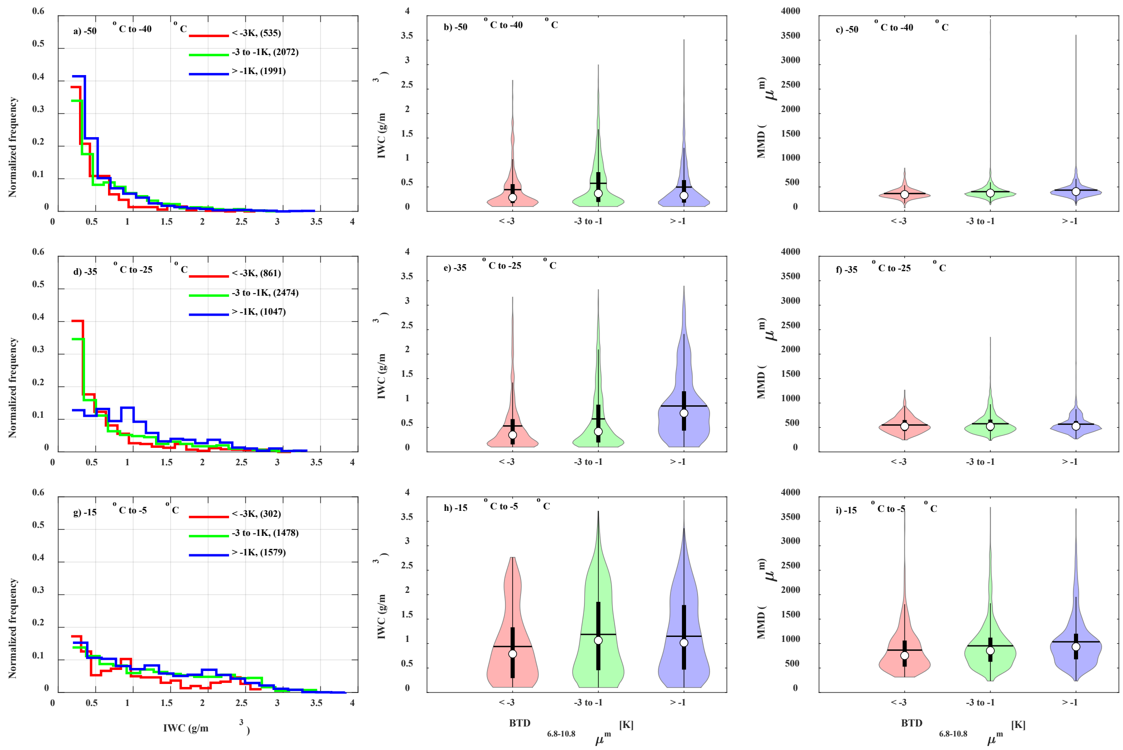

Figure 15. As in figure 3 but for MCSs sorted by $BTD_{6.8\text{-}10.8\mu m}$ (< -3K, -3 to -1K, > -1K) rather than for updrafts, downdrafts and stratiform regions.

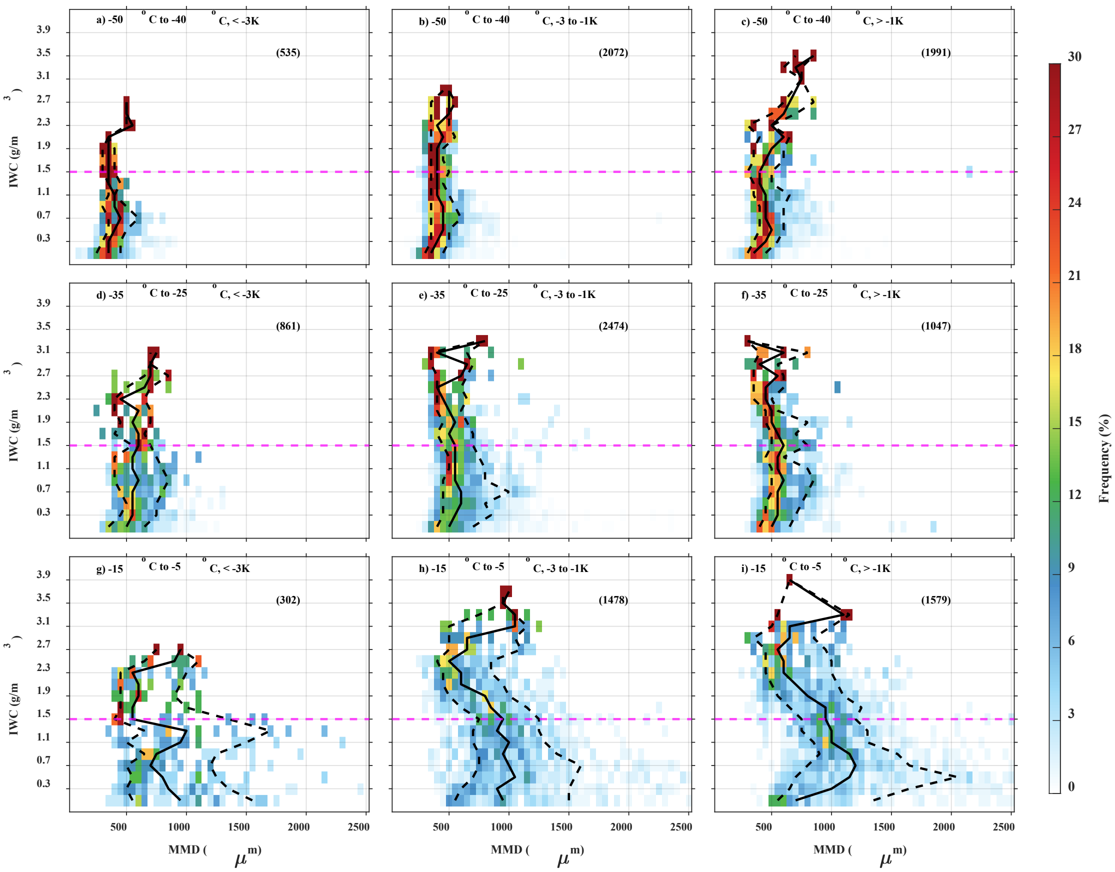

Figure 16. As in figure 4 but for MCSs sorted by $BTD_{6.8\text{-}10.8\mu m}$ (< -3K, -3 to -1K, > -1K) rather than for updrafts, downdrafts and stratiform regions.

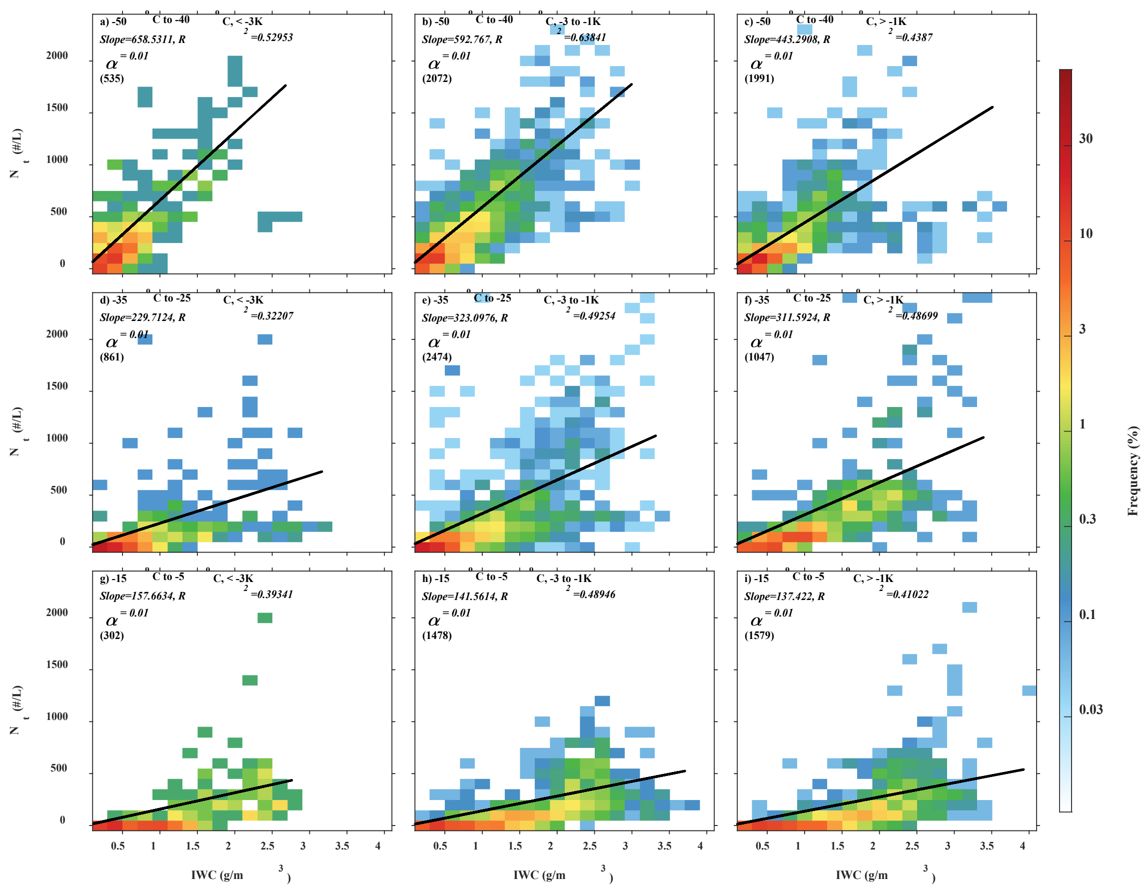

Figure 17. As in figure 5 but for MCSs sorted by $BTD_{6.8\text{-}10.8\mu m}$ (< -3K, -3 to -1K, > -1K) rather than for updrafts, downdrafts and stratiform regions.